COO-3065-334

UR-826

RADIATIVE DECAY WIDTH OF THE ρ^- MESON

T. Jensen, D. Berg, C. Chandlee, S. Cihangir, T. Ferbel,
J. Huston, F. Lobkowicz, M. McLaughlin, T. Ohshima,
C. A. Nelson, P. Slattery, and P. Thompson
University of Rochester, Rochester, N. Y. 14627

and

J. Biel, T. Droege, A. Jonckheere, and P. F. Koehler
Fermi National Accelerator Laboratory, Batavia, IL. 60510

and

B. Collick, S. Heppelmann, T. Joyce, Y. Makdisi, M. Marshak,
E. Peterson and K. Ruddick
University of Minnesota, Minneapolis, MN 55455

THE UNIVERSITY OF ROCHESTER

DEPARTMENT OF PHYSICS AND ASTRONOMY

ROCHESTER , NEW YORK

Radiative Decay Width of the ρ^- Meson*

T. Jensen[(a)], D. Berg, C. Chandlee, S. Cihangir, T. Ferbel, J. Huston,
F. Lobkowicz, M. McLaughlin, T. Ohshima[(b)], C. A. Nelson[(c)],
P. Slattery, and P. Thompson[(d)]

University of Rochester, Rochester, New York 14627

and

J. Biel, T. Droege, A. Jonckheere, and P. F. Koehler

Fermi National Accelerator Laboratory, Batavia, Illinois 60510

and

B. Collick, S. Heppelmann, T. Joyce, Y. Makdisi[(d)], M. Marshak,
E. Peterson, and K. Ruddick

University of Minnesota, Minneapolis, Minnesota 55455

Abstract

We present data on coherent ρ^- production on nuclear targets and our application of the Primakoff formalism for extracting the radiative decay width for the transition $\rho^- \to \pi^-\gamma$. Assuming the presence of both electromagnetic and strong contributions to coherent production, we obtain $\Gamma(\rho^- \to \pi^-\gamma) = 71 \pm 7$ KeV, a result in good agreement with SU(3).

* Research supported by the U. S. Department of Energy and The National Science Foundation.

(a) Presently at EP Division, CERN.
(b) Presently at INS, University of Tokyo.
(c) Presently at Fermilab.
(d) Presently at Brookhaven National Laboratory.

I. INTRODUCTION

Successes obtained in the application of quantum electrodynamics to atomic phenomena and to scattering of leptons would suggest that the photon can serve as a valuable probe for investigating the dynamics of hadronic systems. One such area of study, that is accessible both to experimental observation and direct theoretical interpretation, involves radiative transitions of vector mesons to pseudoscalar mesons ($V \to P + \gamma$). Straightforward predictions for these processes, based on quark models and SU(3) symmetry arguments, are available in the literature[1].

In a simple quark model, the lowest-lying meson states are presumed to be composed of quarks and antiquarks ($q\bar{q}$) in relative S-states. In this scheme the decay $V \to P + \gamma$ is a magnetic dipole transition which can be represented by the operator

$$M = \sum_j \mu_j \vec{\sigma}_j \cdot (\vec{k} \times \vec{\epsilon}) \qquad (1)$$

where the summation is over the quarks in the system, each having magnetic moment μ_j; $\vec{k}$ and $\vec{\epsilon}$ are, respectively, the momentum and polarization of the emitted photon; $\vec{\sigma}_j$ are the Pauli matrices. The radiative decay width is given by

$$\Gamma(V \to P + \gamma) = (\text{phase space factor}) \times \sum |\langle P|M|V\rangle|^2 \ , \qquad (2)$$

where all accessible final states are summed over and an average is taken over the initial states.

Because the wavefunctions for $q\bar{q}$ systems are not very well known, it is necessary to make several assumptions when evaluating Eq. (2). In a nonrelativistic calculation, assuming the long wavelength approximation and complete overlap between the initial and final state spatial wavefunctions, Eq. (2) becomes[2]

$$\Gamma(V \to P + \gamma) = \frac{4}{3} k^3 \mu^2 \frac{E_P}{M_V} \quad , \tag{3}$$

where μ, defined by Eqs. (1) and (2), is the transition moment between the vector and pseudoscalar states; M_V is the mass of the vector particle, and E_P is the energy of the recoiling pseudoscalar in the rest frame of V.

Model dependent assumptions can be avoided to a large extent by calculating ratios between similar processes. For example, assuming ideal mixing for the ω^o, one can calculate the ratio

$$\frac{\Gamma(\rho^- \to \pi^- \gamma)}{\Gamma(\omega^o \to \pi^o \gamma)} = \left(\frac{k_\rho}{k_\omega}\right)^3 \left|\frac{m_\pi^2 + k_\rho^2}{m_\pi^2 + k_\omega^2}\right|^{1/2} \left(\frac{m_\omega}{m_\rho}\right) \left|\frac{\mu_u + \mu_d}{\mu_u - \mu_d}\right|^2 \tag{4}$$

where k_a is the recoil momentum of the photon in the rest frame of the decaying particle a, and μ_i is the magnetic moment of quark i. Assuming that quark moments are proportional to the charges of the quarks, yields the following prediction:

$$\frac{\Gamma(\rho^- \to \pi^- \gamma)}{\Gamma(\omega^o \to \pi^o \gamma)} = 0.107 \quad .$$

(If SU(3) symmetry were exact this ratio would be 1/9.) The previous[3,4] experimental result for this ratio was:

$$\frac{\Gamma(\rho^- \to \pi^-\gamma)}{\Gamma(\omega^o \to \pi^o\gamma)} = \frac{35 \pm 10 \text{ KeV}}{789 \pm 92 \text{ KeV}} = 0.044 \pm 0.014 ,$$

which is over four standard deviations from the prediction. The fact that the ρ and ω masses are nearly equal has made it difficult to introduce a dynamical symmetry breaking which could account for this large discrepancy. It was therefore considered important to remeasure these radiative widths and, especially, the more controversial value of $\Gamma(\rho^- \to \pi^-\gamma)$.

Unlike the transition $\omega^o \to \pi^o\gamma$, where the branching ratio for the decay is relatively large ($\approx$8%) and background from other modes not very serious, the transition $\rho^- \to \pi^-\gamma$ has a branching ratio of $\lesssim 10^{-3}$, and cannot be measured directly, because of the large background anticipated from the predominant decay $\rho^- \to \pi^-\pi^o$, in which one of the photons from the π^o decay is not detected. Studying the inverse reaction $\gamma + \pi^- \to \rho^-$ provides a relatively clean method for determining the decay width $\Gamma(\rho^- \to \pi^-\gamma)$. This can be accomplished, as shown in Fig. 1a, by coupling an incident pion to a virtual photon from the Coulomb field of a nucleus of charge Z (Primakoff effect)[5].

The cross section for this process can be written as a function of the mass of the final state (M) and the square of the momentum transfer to the nucleus (t), as follows:

$$\frac{d\sigma_c}{dt\,dM^2} = \frac{Z^2\alpha}{\pi} \frac{\sigma_\gamma(\gamma a \to b)}{M^2 - m_a^2} \frac{t - t_{min}}{t^2} |F_c(t)|^2 , \qquad (5)$$

where α is the fine structure constant, and $\sigma_\gamma(\gamma a \to b)$ is the cross section for the reaction $\gamma a \to b$. The square of the minimum four-momentum transfer is given by

$$t_{min} \approx (M^2 - m_a^2)^2/4P_a^2 \qquad (6)$$

where m_a and P_a are, respectively, the mass and the laboratory momentum of the incident particle. $F_c(t)$ is the electromagnetic form factor of the nucleus, which contains corrections for scattering and absorption of the initial and final states. When the final state, b, is a narrow resonance of mass m_b the Coulomb cross section takes the form

$$\frac{d\sigma_c}{dt} \equiv |T_c|^2 = 8\pi\alpha Z^2 \frac{2J_b+1}{2J_a+1} \Gamma(b \to a\gamma) \left(\frac{m_b}{m_b^2-m_a^2}\right)^3 \frac{t-t_{min}}{t^2} |F_c(t)|^2 , \qquad (7)$$

where J_a and J_b are the spins of the particles, and T_c is the Coulomb amplitude.

Electromagnetic production is seen from Eq. (7) to be characterized by a very sharp forward peak in the differential cross section. Nevertheless, as a consequence of current conservation for the electromagnetic field[6], the cross section must vanish at $t=t_{min}$. The angular distribution for the decay products of the final state is completely determined by the fact that there is a unit change in the helicity at the top vertex of Fig. 1a. The natural reference frame for describing these coherent processes is the Gottfried-Jackson frame[7], as depicted in Fig. 1b. In this frame the decay $\rho^- \to \pi^-\pi^o$ should follow the form $\sin^2\theta \sin^2\phi$.

Hadronic exchanges can also contribute to the coherent transition a → b. For example, using a pion beam, coherent ρ production can proceed through exchange of the ω^o. However, the form of the cross section is quite different from that for Coulomb production, namely[8]:

$$\frac{d\sigma_s}{dt} \equiv |T_s|^2 = A^2 C_s (t-t_{min}) |F_s(t)|^2 , \qquad (8)$$

where A is the nucleon number, C_s is a normalization factor for production on a single nucleon, and $F_s(t)$ is the hadronic form factor of the nucleus, which, as in the case of $F_c(t)$, contains corrections for rescattering and absorption. T_s defines the amplitude for the ω-exchange contribution to coherent production.

The electromagnetic and hadronic processes can interfere, and we therefore write the cross section for coherent production on nuclei in the form

$$\frac{d\sigma}{dt} = |T_c + e^{i\phi} T_s|^2 , \tag{9}$$

where ϕ is the relative phase between the Coulomb and strong amplitudes.

Because Coulomb production increases logarithmically with the incident beam energy, whereas strong production falls (as $1/P_a$ for ω^o exchange), the strong amplitude, T_s, becomes less important as the incident energy increases, thereby making the extraction of $\Gamma(\rho^- \to \pi^-\gamma)$ less model dependent.

Coherent production of the ρ^-, and of the $\bar{K}^{*o}(890)$ via the Primakoff effect have been observed for incident energies in the range of 8 to 23 GeV.[9] At these energies hadronic exchanges tend to dominate the production process. We have measured the coherent reaction

$$\pi^- A \to A\pi^-\pi^o \tag{10}$$

for different nuclei, at incident beam momenta of 156 GeV/c and 260 GeV/c, where on the contrary, Coulomb production is expected to dominate the coherent cross section.

Initial results from this experiment have already been published.[10] For this paper, which supersedes our previous work, we have reanalyzed the data

and give a detailed account of the method used to measure the radiative width of the ρ^-. In Sec. II we describe the experimental technique employed. The analysis of the data is presented in Sec. III, and in Sec. IV we apply our model, admitting both Coulomb and strong-coherent production, to extract the radiative width $\Gamma(\rho^- \to \pi^- \gamma)$. In Sec. V we compare the results of our studies with theoretical predictions.

II. EXPERIMENTAL TECHNIQUE

A. General considerations

Coulomb production at high energies typically involves momentum transfers of several MeV/c. To clearly observe such processes requires very good angular resolution for both charged and neutral particles. The spectrometer shown schematically in Fig. 2 was constructed with this in mind[11]. Charged-particle trajectories and momenta were measured using a system of drift chambers (DWC) and proportional chambers (MWPC) in conjunction with an analyzing magnet (BM109). This magnet had an aperture of 8 inches by 24 inches, and an integrated field length of 36.74 kGm, corresponding to a transverse impulse of 1.103 GeV/c. Energies and positions of photons were measured using a finely segmented liquid-argon calorimeter.

To minimize background from interactions in material other than the target, and to reduce the effect of multiple-Coulomb scattering on the resolution of charged particles, the target was placed in an evacuated box. For the same reasons a 250-inch-long pipe downstream of the target was also evacuated, and polyethylene bags containing helium gas were placed in remaining spaces between elements of the spectrometer. The evacuated decay pipe provided a region from which we could obtain an

unambiguous sample of $K^- \to \pi^-\pi^0$ decays, which served as a monitor of the performance and acceptance of the spectrometer, and provided a normalization for production cross sections.

Several different nuclear targets were selected to study the scaling properties of electromagnetic and hadronic production processes. Two thicknesses of lead and copper were used to check that we were making proper corrections for target-dependent effects, such as photon conversion and pion absorption. The properties of the targets used in this experiment are presented in Table I. The target thicknesses were chosen mainly to limit the absorption of photons and minimize the effect of multiple-Coulomb scattering on the resolution of charged-particle trajectories.

The experiment was performed at Fermilab in the M-1 secondary beam-line; this beam was produced at an angle of 3.9 mr relative to a 400 GeV/c primary proton beam that impinged on a beryllium target. The incident-particle flux at the experimental target was composed of 94% π^-, 4.5% K^-, and 1.5% $\bar{p}$ at 156 GeV/c, and 98% π^-, 1.5% K^-, and 0.3% $\bar{p}$ at 260 GeV/c. These particle types were identified by means of three Cherenkov counters located upstream of our spectrometer. The beam trajectory was defined by two sets of proportional chambers (J1 and J2), each consisting of two X- and two Y-planes with 1 mm wire spacings. The angle of the beam trajectory was determined to a precision of $\pm$ 0.03 mr.

B. Drift chambers

Each of the DWC modules, D1-D4 in Fig. 2, was composed of three pairs of drift chambers, with members of a pair offset by half of a drift cell with respect to each other (to aid in resolving the ambiguity as to which

side of a sense wire a particle traversed). In modules D1 and D2 sense wires were oriented vertically, horizontally, and $\pm$ 30° to the vertical. The wires in D3 and D4 were oriented vertically and $\pm$ 18.5° to the vertical. The spacing between sense wires in all planes was 0.8 inches.

The drift times of signals from these chambers were digitized relative to a scintillation-counter trigger. Under typical operating conditions one count corresponded to a drift time of about 2 nsec, or to a distance of about 0.1 mm. Given a signal on wire n, the digital count, c_n was converted to spatial coordinate, x, by applying the formula

$$x = x_o + n \cdot s \pm v \cdot (b_n + g_n \cdot c_n) \ , \tag{11}$$

where the two signs indicate the two ambiguities; s is the spacing between sense wires, taken to be 0.8 inch for all wires (the spacings were found to be good to $\pm$ 0.001 inch); x_o is an offset corresponding to the position of the first wire in each plane, and v is the drift velocity of electrons in the gas. The parameters x_o and v were determined by minimizing the χ^2 for straight-line fits to tracks resulting from $K^- \to \pi^-\pi^o$ decays. The calibration constants b_n and g_n correspond, respectively, to an offset and a gain for converting from digital counts in channel n to drift time. Prior to writing each data tape, b_n and g_n were determined for each channel by triggering the electronics with a series of pulses of known relative timing and fitting a linear equation to the resulting data.

From fits to charged tracks from $K^- \to \pi^-\pi^o$ events, the resolution of the drift chambers was determined to be σ = 0.20 mm (standard deviation per plane) for tracks outside the beam region, and σ = 0.26 mm for tracks

in the region of the beam (diameter $\simeq$ 1 cm). This deterioration in resolution in the beam region can be attributed to an accumulation of space charge, which modifies the electric field in the vicinity of the beam. For most of our data, the trajectories of the secondary charged tracks were outside of the beam region and, consequently, this deterioration had only minimal effect on the results. The angular resolution for tracks outside the beam region was $\sim$ .06 mr, and the momentum resolution for charged particles was $\delta p/p \sim 8 \times 10^{-5}$ p (where p is in GeV/c).

C. Liquid-argon calorimeter

The liquid-argon calorimeter (LAC) is depicted schematically in Fig. 3. This detector was composed of alternating layers of 0.080 inch thick lead sheets and 0.063 inch thick copper-clad ($\sim$ 0.001 inch thick Cu) G-10 circuit boards separated by 0.080 inch of liquid argon. The lead sheets were held at a potential of 1.5 kV relative to the copper-clad boards. These circuit boards had 0.5 inch wide strips etched on both sides and oriented horizontally or vertically on alternate boards. The vertical strips extended the full lengths of the boards, while the horizontal strips were separated into left and right halves. A total of 61 cells were assembled, providing a thickness of 24.5 radiation lengths and 1.6 proton-interaction lengths. The detector was divided into front/back and left/right sections. Within each section all strips with the same X or same Y coordinate were connected to a single amplifier so as to sum the energy along the Z direction.

When the event trigger was satisfied, each amplifier channel was sampled for pulse height information at two times that were separated by

400 nsec (the intrinsic risetime of the input signal was approximately 250 nsec). The difference between these two levels was taken to be proportional to the energy deposited in that LAC strip.[12] Signals above a preset threshold, corresponding to a calibrated energy deposition of about 100 MeV per channel, were digitized and written onto data tape.

The LAC amplifiers were tested and calibrated before each data run. A signal of known amplitude was applied to the input of each channel to measure the gain of the amplifier, and a pedestal (offset) was measured by temporarily setting the digitization threshold to zero. From these measurements it was determined that no time-dependent correction was necessary for the gains. Pedestal levels were subtracted from the digitized level for each channel on an event by event basis.

In order to determine the absolute value of the gain for each channel, calibration data were taken with the beam momentum set to 50 GeV/c and one of the Cherenkov counters tuned to identify electrons. The drift chambers and the BM109 magnet were used to determine the momentum of the electrons to compare with the energy measured in the LAC.

Additional checks of the performance of the LAC were provided by studies of electron-Bremsstrahlung events accumulated during normal data taking. The energy resolution of the LAC is indicated in Fig. 4a. The dashed line corresponds to a resolution $\sigma_E^2 = 0.18 + (0.20)^2 E$ (where E is in GeV). These electron data were used to align the LAC with respect to the rest of the spectrometer, as well as to measure the position resolution of the LAC. Figure 4b shows a distribution for the difference between the position of an electron as calculated by the LAC (X_{LAC}), and as predicted by the drift chambers (X_{DC}). (The algorithm used to determine X_{LAC} is described in Sec. III.B.) Taking the drift-chamber resolution into account implies a

spatial resolution for the LAC of ∿0.7 mm (standard deviation per projected coordinate).

D. Trigger electronics

The trigger for the experiment was designed to select coherent interactions that had one charged particle and at least one photon in the final state. The arrangement of counters used to define the trigger is depicted schematically in Fig. 5. The incident beam was defined by the coincidence B0•B1•B2•B3•$\overline{BH}$. The counter BH had a 0.625 inch diameter hole centered on the target. The B2•B3 coincidence was used to form a $\pm$ 200 nsec deadtime gate around the trigger pulse. This was done in order to minimize difficulties in reconstructing data from the drift chambers. The digitizers were capable of recording only one hit per drift wire per trigger, which meant that a second particle that appeared within the 200 nsec drift-time interval could produce hits not associated with the event of interest. Requiring a separation of 200 nsec between beam particles contributed about 10% deadtime in the trigger for B2•B3 intensities of 3×10^5 particles per second.

The inset in Fig. 5 shows the arrangement of counters surrounding the target. For coherent interactions, entire nuclei recoil with typical momenta of less than 100 MeV/c; such momenta are not high enough for the nuclei to leave the target. To enhance triggers from reactions of this type, we used counters composed of sandwiches of lead and scintillator (V1-V4 and H) in veto. This suppressed the majority of interactions which involved multiparticle production and nuclear breakup. The S-counter, located eight inches downstream of the target, was used to determine the number of charged particles leaving the target in the forward direction. Minimum and maximum

discriminator levels were set to select events that had one charged particle emerging from the target. This entire assembly was housed in an evacuated box. Additional sandwiches of lead and scintillator, A1, A2, and AM, were used as vetos to define the geometrical acceptance of the spectrometer; this was basically limited by the aperture of the analyzing magnet.

Because the targets we used were typically a few percent of a collision length thick, most of the beam passed through them without interacting. The BA counter, a 1.125 inch diameter scintillator, placed just in front of the LAC, was used to veto events that had charged particles in the region of the unscattered beam. In addition, for much of the data, the BA veto was supplemented by a larger veto counter (VE). This (two inch high by four inch wide) counter suppressed additional background triggers due to small angle elastic scattering in the target.

Material downstream of the target (chambers, scintillation counters, etc.) corresponded to a total thickness of $\sim$0.03 of a collision length; this was comparable to the thickness of the target. Triggers due to interactions in this material were not rejected efficiently enough by the BA and VE counters. To suppress such unwanted events, we formed a matrix between the signals from the X-planes of the beam chambers (J1 and J2) and the central 1.2 inch region of the proportional chamber located just downstream of the decay pipe (P1). An event was vetoed whenever the matrix requirement was satisfied; namely, when the angle of the outgoing track (in P1) deviated by less than 0.3 mr from the beam track (as defined by the X-projection of the J chambers). To prevent rejection of particles that had a small angle in the X-projection but a large scattering angle in the vertical plane, a one inch diameter counter, BV, was placed just downstream of the P1 chamber and required to be in coincidence with the matrix signal if the event were to be vetoed.

In order to restrict triggers to those with one charged particle in the final state, fast logic signals were formed using the P1 and P2 chambers to count the number of charged tracks that passed through the apparatus. Signals from the two offset planes in each chamber were interleaved to reduce the effective wire spacing by a factor of two. A track was defined by the presence of signals on a contiguous group of these interleaved wires, if the group was separated from neighboring groups by at least one signal-less wire. The trigger was satisfied when either one or two tracks were found in the P1 system, and one, two, or three tracks in the P2 system. We used such conservative requirements in order not to be sensitive to background due to noise pulses, δ-rays, and, in P2, ambiguities due to tracks that traversed this chamber at large angles.

To satisfy the full ρ trigger, in addition to the charged-track criteria, more than 10 GeV of energy was required to be deposited in the front part of the LAC. However, this requirement alone was not restrictive enough in that it admitted a sizeable fraction of triggers from elastically scattered beam particles that interacted in the LAC. To suppress this background we invoked momentum conservation for decays of the type $\rho^- \to \pi^-\pi^o$. Coulomb production of the ρ^- is essentially along the direction of the beam; hence, if the decay π^- is emitted above the center-line of the apparatus, the π^o must appear below the center-line, and vice versa. A wall of up (U) and down (D) counters (U1, U2, U3; D1, D2, D3 in Fig. 5) was set up to cover the active area of the LAC, and to determine whether the trajectory of a charged particle was above or below the center-line. Fast differential outputs from the LAC amplifiers were added together for the upper and lower Y-strips in the front half of the detector and discriminated to form signals indicating

energy deposition in the upper or lower half. The trigger was accepted when $\gtrsim$ 10 GeV of energy was deposited in the upper (lower) half of the LAC, but only if there was no simultaneous signal present in the U (D) counters.

Data were accumulated using a CAMAC system interfaced to a DEC PDP-15 computer. This computer also controlled monitoring and calibration of the drift chambers and of the LAC system. Data were recorded concurrently for three different kinds of triggers; the trigger type was latched so that all information could be sorted out at the off-line analysis stage. Different targets (see Table I) were alternated throughout the running period and additional triggers were taken with no target present (for background subtraction). The integrated beam flux in the experiment was 2.2×10^9 π^- and 1.0×10^8 K^- at 156 GeV/c, and 0.79×10^9 π^- and 0.13×10^8 K^- at 260 GeV/c.

III. DATA ANALYSIS

A. Charged-track reconstruction

The coordinates measured in the drift and proportional chambers were fitted to straight-line segments (one segment using the beam chambers, one the chambers upstream of the analyzing magnet, and one using the chambers downstream of the analyzing magnet). The segments on either side of the magnet were constrained to intersect at the center of the magnet and to have the same slope in the vertical coordinate. (The uniformity of the magnetic field of the BM109 magnet was sufficient to justify these approximations.)

As a result of the two-fold ambiguity between drift time and position, each drift chamber produced two possible coordinates for a single track. These were treated on equal footing in the reconstruction process, and the

fit that yielded the best χ^2 was chosen to define the trajectory of the particle. The particle's momentum was calculated from the difference between the horizontal slopes of the track segments upstream and downstream of the magnet; that is, $p = 1.103\ (\text{GeV/c})/(\sin\theta' - \sin\theta)$, where θ and θ' are the horizontal entrance and exit angles of the track through the magnet, and 1.103 GeV/c is the transverse impulse produced by the magnetic field. The vertex for the interaction was defined by the point of closest approach between the trajectories of the beam track and the outgoing charged track.

B. Photon reconstruction

During the initial stages of photon reconstruction, the X and Y projections of the LAC were treated independently. The strips that had signals above 100 MeV were interrogated to find local maxima (peaks) in energy deposition. Pulse heights from three neighboring strips centered on a peak were used to calculate a coordinate and an energy for a candidate photon in that projection. For pulse heights denoted as P1, P2, P3 (with P2 being the largest), the projected energy was defined by $E = b\,(a(P1 + P3) + P2)$, where a and b are constants which were determined empirically using electron-calibration data. The position of the photon relative to the center of the P2 strip was given (in units of the strip width) by

$$X = \pm[0.4 + A(C1 \mp \sqrt{C2 + C3/A^2})\ ]\ ,$$

where $A = |P3 - P1|/P2 - C4$, and C1, C2, C3, and C4 are constants determined once again, using electron-calibration data.

A photon was fully reconstructed whenever the energies from the two projections, E_X and E_Y, agreed to within an empirically determined tolerance given by

$$\frac{|E_X - E_Y|}{[E_X + 0.5 + 0.03\ E_X^2]^{1/2}} < 0.5$$

A second iteration of this procedure was needed to reconstruct events in which showers from two photons overlapped in one view. In this case, the energy from a shower in one projection was required to agree with the summed energy from the two showers in the other projection.

After making all allowed correlations, the energies from the two projections and from the corresponding strips in the back half of the detector were added together to define the total energy of each photon. The position of each photon was determined, as described above, using only the information from the front half of the detector in each projection. Photon positions were compared with the position of the charged track, extrapolated to the front of the LAC, and those photons that matched up with the charged track (within 0.75 inches) were flagged as being electron candidates or interacting hadrons.

C. Monte Carlo model

The reconstruction algorithms for the LAC and track chambers were checked using $K^- \to \pi^-\pi^o$ events. These decays have quite similar kinematics to $\rho^- \to \pi^-\pi^o$ decays; hence, a comparison of the observed yield of $K^- \to \pi^-\pi^o$ events, to that predicted, provides a good means for normalizing the production cross section for $\rho^- \to \pi^-\pi^o$ events. Differences in the efficiency for detecting the two reactions were calculated via a Monte Carlo program.

Kinematic variables for the respective reactions were generated using known masses and expected decay-angular distributions. A beam trajectory was selected from a distribution matching that of the data. Multiple-Coulomb scattering of charged particles passing through the target material was included, assuming a Gaussian approximation.[13] The limits of the magnet aperture and of the various scintillation counters used in the trigger, as determined from the observed boundaries in distributions of the reconstructed positions of charged particles, were used to establish a fiducial region for the acceptance of the apparatus.

Trajectories for generated charged particles were converted to sets of hits in the proportional and drift chambers, taking account of the measured efficiency, resolution, and noise rate in the chambers.

Energy was deposited in those strips of the LAC which were struck by generated photons, electrons, or hadrons. The lateral and longitudinal deposition of energy was simulated to reproduce the distribution observed in our studies of electrons and pions that showered in the detector.

The generated events were then checked to ascertain that they satisfied the requirements of the trigger (see Sec. II.D), and the track chamber and LAC information was then reconstructed using the same algorithms as used for reconstructing data collected during the experiment.

D. $K^- \to \pi^-\pi^0$ and $K^- \to e\bar{\nu}\pi^0$ Decays

Comparisons were made between Monte Carlo predictions and data for $K^- \to \pi^-\pi^0$ decays. Several of these comparisons are presented below, both for data at 156 GeV/c and at 260 GeV/c. The beam particles for these events were identified as kaons using the Cherenkov counters. Small background

from K_{e3} decays that contaminated the $K_{2\pi}$ sample was suppressed by using the LAC to tag the electron. In particular, charged tracks with measured momenta that agreed to within 10% with the energy deposited in the LAC, and with extrapolated positions (from DWC's to LAC) that agreed to within 0.75 inches with the position of the accompanying shower in the LAC, were defined as electrons.

Figure 6 shows the two-photon mass spectra for the $K_{2\pi}$ candidate events. The solid curves are predictions of the Monte Carlo model. Events with two-photon masses between the arrows in Fig. 6 were assumed to be π^o's. Distributions in the summed energy of the π^- and the two photons for events satisfying this π^o mass requirement are presented in Fig. 7. The momentum spread of the beam was $\lesssim$ 1%, hence, the widths of these distributions can be attributed mainly to the resolution of the spectrometer. The excess of events at low energies is predominately due to remnant $K_{\mu 3}$ and K_{e3} background. To further reduce this background, events in the $K^- \to \pi^-\pi^o$ signal were required to have a restricted total energy as indicated by the arrows in Fig. 7. (Both Figs. 6 and 7 have vertex requirements on the reconstructed tracks, which are described below.)

Figure 8 shows reconstructed decay-vertex distributions for $K^- \to \pi^-\pi^o$ events which satisfied the two-photon mass and total energy requirements. The sharp falloff at the downstream end of the decay pipe was caused primarily by the matrix-beam-veto requirement in the trigger. Losses near the origin were caused principally by the veto counters surrounding the target. In order to avoid any possible difficulties associated with these end regions, only those events which had decay vertices between the arrows (35 inches to 135 inches at 156 GeV/c, and 35 inches to 185 inches at 260 GeV/c) were

selected for studying the resolution of the apparatus and for normalizing production cross sections. The discrepancy near the origin between the Monte Carlo and the data is due to the fact that the veto counters surrounding the target were not included in the Monte Carlo.

Distributions in the $\pi^-\pi^o$ invariant mass are shown in Fig. 9 for events satisfying the previously mentioned restrictions on the vertex, the two-photon mass and the total energy. Again, the smooth curves are Monte Carlo predictions, normalized to the total number of events in the distributions. The $\pi^-\pi^o$ mass resolution for these decays is 10 MeV (standard deviation) at 156 GeV/c and 12 MeV at 260 GeV/c. The $K^- \to \pi^-\pi^o$ signal was defined using the mass limits indicated by the arrows in these plots. In summary, $K^- \to \pi^-\pi^o$ decays were selected using the following restrictions: 1) kaon Cherenkov signal for the incident track, 2) acceptable decay vertex, 3) charged track not consistent with being an electron, 4) acceptable two-photon mass, 5) expected total energy, and 6) acceptable $\pi^-\pi^o$ mass.

Studies of additional kinematic quantities were made for events satisfying the above restrictions. For example, Fig. 10 shows distributions for the square of the distance (R^2) of the π^- trajectory in drift chamber D1 relative to the position of the beam trajectory extrapolated to D1. The Monte Carlo model is in good agreement with the data, even in the vicinity of the beam ($R^2 \lesssim 0.1$ in^2), where the efficiency and resolution of the chambers deteriorates somewhat.

Distributions in the energy asymmetry, $|E_{\gamma 1} - E_{\gamma 2}|/(E_{\gamma 1} + E_{\gamma 2})$, for the two photons from the decay $\pi^o \to \gamma\gamma$ are compared with the Monte Carlo predictions in Fig. 11. Because a π^o decays isotropically in its rest frame, these distributions would also be expected to be isotropic; however, losses of low energy ($\lesssim$8 GeV) photons cause the fall-offs observed at large asymmetries.

Angular distributions for $K^- \to \pi^-\pi^o$ decays are presented in Fig. 12. The angle θ is that of the charged pion relative to the flight direction of the kaon, as measured in the rest frame of the kaon (helicity axis). Because the kaon has no spin, its decay-angular distribution should be isotropic. Poor acceptance in the region of large $\cos\theta$ corresponds to losses of charged tracks due to the vetoing by the matrix-beam-veto, as well as to losses due to vetoing (and inefficiency for reconstructing) of low energy π^o's. Once again, the Monte Carlo curves are in good agreement with the data.

A comparison of the t-resolution for the $K^- \to \pi^-\pi^o$ signal for different targets and different beam momenta is presented in Fig. 13. (If the resolution of the spectrometer were perfect, we would expect all K-decays to occur at t=0.) The effect of multiple-Coulomb scattering in the individual targets is clearly observed in Fig. 13 and agrees well with expectations.

K_{e3} decays were also studied in this experiment. As indicated above, the electron was identified using the LAC. The decay-vertex distribution and the electron momentum spectrum for events having an identified electron and an acceptable π^o are shown in Figs. 14a and 14b, respectively. The matrix elements for K_{e3} decay, listed in the recent Particle Data Tables[13], were used in generating the Monte Carlo events. The same acceptance model that was used for $K^- \to \pi^-\pi^o$ decays produced good agreement between the K_{e3} data and the Monte Carlo predictions.

E. Corrections to the data

The Monte Carlo model did not include corrections for processes such as decays or secondary interactions of particles in the target or in the material of the spectrometer. However, these losses depend only on the

event topology, and can be categorized as follows: (1) beam related corrections, (2) target-dependent corrections, and (3) corrections related to the design and performance of the spectrometer. Multiplicative correction factors used for these items are described below.

(1) Beam-related corrections

The procedure used for measuring the incident beam flux was described in Sec. II. Corrections were applied to account for decays and interactions of beam particles, and for misidentification of particles by the Cherenkov counters. These (generally small) correction factors for different beam particles and incident momenta are listed in Table II.

(2) Target-dependent corrections

The yields were corrected for absorption of charged particles and photons in the target, and for triggering losses caused by δ-rays produced in the target. (Refer to Table I for a summary of properties of the targets.)

The effect of losses due to δ-rays was measured for only one target (Cu-2), and the results extrapolated to the other targets. To measure the veto rate caused by this source, a trigger was implemented that required beam particles to pass the target and strike the BA counter, (see Fig. 5). The coincidence rate between the counters V1-V4 and the BA counter was interpreted as the veto rate due to δ-rays produced in the target. (A small correction of 0.5% was made for random firing of the V1-V4 counters.) The measurement for the Cu-2 target indicated that $4.1 \pm 0.5\%$ of all beam-like tracks produced δ-rays that would veto good events. Because of differences in multiple-Coulomb scattering, extrapolation of this rate to the other

targets was somewhat uncertain. Nevertheless, because all targets were of similar thickness, the correction factors for δ-ray vetos (summarized in the second column of Table III) were estimated to be accurate to ±2%.

Using the approximate formula: $N(\ell)=N_o \exp(-7\ell/9)$,[14] where ℓ is the number of radiation lengths of material in the path of the photon, a correction was calculated for the loss of photons through conversion to electron-positron pairs. For interactions occurring in the target, ℓ was taken to be half of the target thickness. The third column of Table III lists the correction factors that were applied to events in which a π^o (two photons) originated in the target.

In order to account for differences in nuclear absorption cross sections for different types of incident particles, the data of Allaby et al[15] were used to calculate the correction factors for charged-particle absorption in the targets. These are listed in Table III.

(3) Spectrometer-related corrections

The remaining kinematics-independent corrections that we considered are described briefly in Table IV. Additional small losses that may have been present because of possible inefficiencies in the electronics have been ignored because such losses had similar effects on all of the data, and would be automatically corrected through the normalization of yields to $K^- \to \pi^-\pi^o$ decays.

A check of the reliability of the correction factors, and of the Monte Carlo model for the acceptance, is indicated in Fig. 15, where ratios of the observed to the expected number of K-decays are plotted for different targets and energies. Production cross sections for $\pi^-\pi^o$, $K^-\pi^o$ and $p\pi^o$ final states were normalized by dividing the observed yields by these ratios.

The cross section for one interaction can be written as follows:

$$\sigma(\text{per event}) = \frac{A}{N_o \rho t} \frac{(C.F.)}{(\text{incident flux})}$$

where $N_o = 6.02 \times 10^{23}$ is Avogadro's number, and ρt is the thickness of the target in gm/cm^2. The correction factor (C.F.) includes the terms listed in Tables II, III, and IV, the geometric acceptance (averaged over any particular range of kinematics, e.g., a $\pi^-\pi^o$ mass interval), and the normalization to the yield of K-decays.

F. $\Delta^+(1232)$ Production

To check our application of the Primakoff formalism to the ρ^-, we investigated Coulomb production of the $\Delta^+(1232)$ resonance, in which case the radiative width is known. In order to obtain sufficient statistics for this study, several data runs were taken using a positively charged beam. The results were compared with predictions of the Primakoff formula based on input from the photoproduction reaction $\gamma p \to p\pi^o$.[16,17] The cross section for the latter process is dominated by the $\Delta^+(1232)$ resonance, and agreement between our data and predictions from the photoproduction measurements would lend further credence to the reliability of our measurement of the radiative width of the ρ^-.

Events selected as candidates for coherent $p\pi^o$ production satisfied the same restrictions on the two-photon mass and total energy as were used for selecting K-decays. An incident-proton signal was required in the Cherenkov counters, and the interaction vertex was required to be within 25 inches of the target. Coherent production of $p\pi^o$ systems on nuclear targets is complicated somewhat by the presence of background from diffractive production.

The Coulomb process, which is our primary concern, dominates at small momentum transfers (t). But just as in the case of ρ^- production, where other exchanges (ω^o and A_2) contribute at larger values of t, diffractive production contributes significantly to coherent production of low-mass $p\pi^o$ systems at larger momentum transfer.[18] The diffractive process, which involves mainly no isotopic spin exhange, can, in principle, be separated from resonant P_{33} Coulomb production by means of a partial wave analysis; but this requires substantially more data than we had available. Therefore, in order to emphasize Coulomb production, we restricted the $p\pi^o$ data sample to those events having $t < 0.001$ GeV^2.

The correction factors from Tables II, III, and IV (for a proton beam and a $p\pi^o$ final state), the $K^+ \to \pi^+\pi^o$ normalization factor, and the Monte Carlo generated acceptance were applied to the $p\pi^o$ data sample. The measured differential cross section is shown in Fig. 16a as a function of mass. Figure 16b shows the mass-dependent acceptance of the spectrometer for the decay of a $J = 3/2$ state produced at small t through photon exchange. The solid curve in Fig. 16a was obtained by substituting the cross section $\sigma_\gamma(\gamma p \to p\pi^o)$ measured by Fischer et al.[16], into Eq. (5) and integrating over t. In performing this integration, it was necessary to account for the resolution of the spectrometer. Uncertainties in the cross section for $\gamma p \to p\pi^o$ and in the resolution limited the accuracy of the comparison to about 10%. (The resolution extrapolated from that found for $K^+ \to \pi^+\pi^o$ decays was used in these calculations.) The data points at the low-mass end of the spectrum tend to be ∿20% above the prediction. In this region the acceptance is poor, and, as a result, the measured cross section is very sensitive to the parameters used in the Monte Carlo. Nevertheless, the integrated cross section for the range 1.13 GeV $< M_{p\pi^o} <$ 1.4 GeV is only 11% above the predicted values.

The decay-angle distribution of the Δ^+ events is shown in Fig. 16c, along with the Monte Carlo prediction. The data selected for this plot were restricted to the mass interval 1.14 GeV < $M_{p\pi^o}$ < 1.28 GeV, and to t < 0.001 GeV^2. For pure Δ^+ production, ignoring acceptance, the distribution should have the form $1+(3/2)\sin^2\theta$. Incoherent background from an S_{11} term would be isotropic, and background from diffractive production would depend strongly on mass and momentum transfer.[18] We regard these results as consistent with Δ^+ dominance of the data for t < 0.001 GeV^2 and $M_{p\pi^o}$ < 1.28 GeV.

This check has therefore provided further confidence in our normalization procedure. Even for the kinematically sensitive region of Δ^+ production and decay (low-momentum π^o and very high-momentum p) we have obtained results which are consistent with expectations at the 10% level.

G. $\pi^- A \to A\pi^-\pi^o$

The sample of $\pi^-\pi^o$ events from Reaction (10) was required to have two-photon masses and total energies within the same limits used to define $K^- \to \pi^-\pi^o$ decays. Figure 17 shows distributions for the reconstructed interaction vertexes for these events for the Pb-2 target. Corrections have been made for target-empty background, present at a level of ≈3% for the Pb-2 target. To satisfy Reaction (10), the data were required to have reconstructed vertexes between the positions indicated by the arrows in these plots (±15 inches at 156 GeV/c and ±20 inches at 260 GeV/c). The solid curves are Monte Carlo predictions, using the same parameterization of the spectrometer as was used for $K^- \to \pi^-\pi^o$ decays. The ρ^- Monte Carlo events were generated at small t according to the steep distribution $e^{-6000t}+1.27\ e^{-1280t}$, with a mass spectrum expected from Primakoff production. (The acceptance was found to be

essentially independent of t for $t < 0.1$ GeV^2.) The decay of the ρ^- was generated according to the expected $\sin^2\theta\sin^2\phi$ form in the Gottfried-Jackson frame.

Figure 18 displays $\pi^-\pi^o$ mass distributions for different nuclear targets at the two energies. These events satisfy the restrictions outlined in the previous paragraph. All spectra exhibit prominent peaks at the mass of the ρ^- and show little evidence of background from other processes. Exceptions are the distribution for the Cu-1 target at 156 GeV/c and distributions for the 260 GeV/c data; these show an additional peak at $\sim$0.5 GeV caused by $K^- \to \pi^-\pi^o$ events for which the incident K^- was improperly tagged as a π^- by the Cherenkov counters. To avoid this background, we required that the $\pi^-\pi^o$ mass for the ρ^- sample be within the limits of 0.55 GeV and 0.95 GeV, and subsequently corrected the cross section for events removed by this restriction.

Distributions in the reconstructed energy of $\pi^-\pi^o$ systems are shown in Figs. 19a, 19b, and 19c for carbon, copper, and lead targets, respectively. All events satisfy the vertex and two-photon mass requirements. The data are shown both for no restriction on t, and for $t < 0.002$ GeV^2 (the shaded areas). Inelastic background is evident in the low energy tail of the distributions. The most likely source of such background would be coherent $A_1 \to \pi^-\pi^o\pi^o$ production in which one of the π^o's was not detected or was improperly reconstructed. The good energy resolution of our apparatus allowed us to eliminate most of this background by requiring that the total energy of the $\pi^-\pi^o$ system be between the values indicated by the arrows in Fig. 19. From studies of these distributions we have estimated that, for the worst case (carbon target), the inelastic background is $\lesssim$3% of the coherent signal for $t < 0.002$ GeV^2.

Further evidence that the ρ^- signal is produced coherently is provided by the decay-angle distributions shown in Figs. 20a and 20b. In addition to the cuts used to define the ρ^- signal, these data have been restricted to have $t < 0.002$ GeV^2. The results are in excellent agreement with the $\sin^2\theta$ form expected for the decay of coherently produced ρ^- mesons. At small values of t, the ϕ dependence is dominated by the resolution of the spectrometer, thus the data for Coulomb production do not clearly display the expected $\sin^2\phi$ distribution. However, data on carbon contain a significant contribution from coherent strong production at larger values of t, and, as seen in Fig. 20c, the distribution for these data agrees quite well with expectations.

The correction factors applied to $\pi^-\pi^o$ data for different targets and different energies are given in Table V, along with the values of the cross section per event. In this table, the geometric acceptance has been averaged over the mass interval $0.55 \text{ GeV} < M_{\pi^-\pi^o} < 0.95 \text{ GeV}$. The small difference in the geometric acceptance for the two targets in the 260 GeV/c data is due to minor differences in the size of the VE counter used in the trigger.

Differential cross sections for ρ^- production on different nuclear targets are shown in Fig. 21. The distributions have been corrected using the factors in Table V, and a background subtraction was performed using data taken without a target in position (target empty). The sharp forward peak, increasing roughly as Z^2 for different targets, indicates that ρ^- production is dominated by the Coulomb process.

IV. FITS TO A MODEL FOR COHERENT PRODUCTION

We have applied the standard optical model for the nucleus[19] to fit the differential cross sections shown in Fig. 21. To emphasize the relevant parameters that will be extracted from the fits, namely Γ_γ, C_S and ϕ, we rewrite Eq. (9) in the following form:

$$\frac{d\sigma}{dt} = \left| \Gamma_\gamma^{\frac{1}{2}} f_C(t) + e^{i\phi} C_S^{\frac{1}{2}} f_S(t) \right|^2 \quad . \tag{12}$$

The target-dependent amplitudes, f_C and f_S, were calculated as described below.

The amplitude for nuclear Coulomb production of a narrow resonance is given by Eq. (7). However, for ρ^- we must use the more general expression given by Eq. (5), in which we substitute the form of a relativistic Breit-Wigner resonance:[20]

$$\sigma_\gamma(\gamma\pi \to \pi\pi) = \frac{8\pi M^2}{(M^2-m_\pi^2)^2} \frac{2J_\rho+1}{2J_\pi+1} \frac{m_\rho^2 \Gamma(\rho \to \pi\gamma)\Gamma(\rho \to \pi\pi)}{(M^2-m_\rho^2)^2+m_\rho^2\Gamma^2(\rho \to \text{all})} \tag{13}$$

$\Gamma(\rho \to \text{all})$, $\Gamma(\rho \to \pi\gamma)$ and $\Gamma(\rho \to \pi\pi)$ are, respectively, the mass dependent total width, and the partial widths for the decays $\rho \to \pi\gamma$ and $\rho \to \pi\pi$. These widths can be rewritten in terms of the widths at resonance, as follows: $\Gamma(\rho \to \pi\gamma) = \Gamma_\gamma g_\gamma(M)$ and $\Gamma(\rho \to \pi\pi) = \Gamma_\rho g_\rho(M)$, where $g_\gamma(m_\rho) = g_\rho(m_\rho) = 1$. (For the case of the ρ we may take $\Gamma(\rho \to \text{all}) = \Gamma(\rho \to \pi\pi)$.) Inserting these formulas into Eq. (5) and integrating over M^2 yields:

$$\frac{d\sigma}{dt} = 8\pi\alpha\, Z^2\, \frac{2J_\rho+1}{2J_\pi+1}\, \Gamma_\gamma$$

$$\times \int dM^2\, \frac{M^2}{(M^2-m_\pi^2)^3}\, g_\gamma(M)\, g_\rho(M) \left[\frac{1}{\pi}\, \frac{m_\rho \Gamma_\rho}{(M^2-m_\rho^2)^2+m_\rho^2 g_\rho^2(M)\Gamma_\rho^2}\right] \frac{t-t_{min}}{t^2} \left|F_C(t)\right|^2 \qquad (14)$$

Note that in the limit $\Gamma_\rho \to 0$ the Breit-Wigner formula becomes a δ-function and we regain Eq. (7).

The M-dependence of the term $(t-t_{min})\left|F_C(t)\right|^2/t^2$ is very weak; we consequently used the form of Eq. (5) for the Coulomb amplitude and applied a correction factor to account for the finite width of the ρ^-. This correction factor was obtained by integrating numerically over dM^2 in Eq. (14). For the energy dependence of the widths we used[20]

$$g_\gamma(M) = \left(\frac{k}{k_o}\right)^2 \frac{2k_o^2}{k^2+k_o^2}\,,$$

$$g_\rho(M) = \left(\frac{q}{q_o}\right)^3 \frac{2q_o^2}{q^2+q_o^2}\,, \qquad (15)$$

where k and q are the momenta in the $\pi\gamma$ and $\pi\pi$ rest frames, respectively. (Values at resonance are subscripted with a zero.) Substituting values for m_ρ and Γ_ρ from the Particle Data Tables[13] into Eq. (14) produces the correction factor, $C_{f\omega} = 0.87 \pm 0.02$, for the finite width of the ρ^-.

Fits were made to the $\pi^-\pi^o$ mass spectrum for events at $t < 0.002$ GeV^2 using Eq. (15) as well as other forms for the energy dependence. We did not have sufficient statistics to clearly establish the parameterization for the ρ-line shape. However, all fits with acceptable χ^2 values gave

similar values for the mass and total width of the ρ.[21] Results using Eq. (15) are shown in Fig. 22 for data on lead at 156 GeV/c and 260 GeV/c. The arrows in these plots indicte the regions used in the fits. The resulting values were, $m_\rho = 767 \pm 3$ MeV and $\Gamma_\rho = 140 \pm 10$ MeV at 156 GeV/c, and $m_\rho = 773 \pm 4$ MeV and $\Gamma_\rho = 150 \pm 10$ MeV at 260 GeV/c. The errors indicated here are statistical only. There is an additional systematic uncertainty of ± 4 MeV in the value for m_ρ.

Using the finite-width correction, and following the formalism given in Ref. 19, we can rewrite the Coulomb amplitude as follows:

$$f_C(t) = \left[24\pi\alpha Z^2 C_{f\omega}\left(\frac{m_\rho}{m_\rho^2 - m_\pi^2}\right)^3\right]^{1/2} F_C(q) \qquad (16)$$

where q is the four-momentum transfer (q^2=t). Defining $\hat{q}_T$ as a unit vector along the transverse part of the momentum transfer vector $\vec{q}$, the electromagnetic form factor of the nucleus, which is just the Fourier transform of the charge distribution, may be written in terms of the electric field, $\vec{E}(\vec{r})$, of the nucleus as follows:

$$F_C(q) = \frac{1}{4\pi i}\int d^3r \psi_f^* \, e^{i\vec{q}\cdot\vec{r}} \hat{q}_T \cdot \vec{E}(\vec{r}) \psi_i \qquad (17)$$

ψ_i and ψ_f^* are, respectively, the incoming π^- and outgoing ρ^- wavefunctions, in the form of Coulomb-distorted plane waves, modified to account for absorption and scattering inside the nucleus. (Note that $q^2 \simeq |\vec{q}|^2$.)

For performing the integration, the z axis is defined by the beam direction, and the transverse coordinate is referred to as the impact parameter, b. Absorption is introduced using the nuclear thickness function, T(b):

$$\sigma'_{\pi}T(b) = \sigma'_{\pi} A \int_{-\infty}^{\infty} dz\, g(b,z),$$

where $g(b,z)$ is the density distribution for nuclear matter. $\sigma'_{\pi} = (1-i\alpha)\sigma_{\pi}$, where σ_{π} is the total π-nucleon cross section, and α is the ratio of the real to imaginary part of the forward scattering amplitude for π-nucleon collisions. (In our calculations we have assumed $\sigma_{\rho} = \sigma_{\pi}$.)[22] Elastic scattering in the nuclear Coulomb field will introduce an additional phase given by

$$\chi_C(b) = -z\alpha \int_{-\infty}^{\infty} dz\, \Phi(\sqrt{b^2 + z^2}),$$

where $\Phi(\vec{r}) = \int d^3r' g(\vec{r}')/|\vec{r}-\vec{r}'|$ is the Coulomb potential of the nucleus.

Assuming $g(\vec{r})$ to be spherically symmetric, we obtain from Eq. (17):

$$F_C(q) = 4\pi \int_0^{\infty} db\, b^2\, J_1(bq_T) e^{-\sigma'_{\pi}T(b)/2}\, e^{i\chi_C(b)}$$

$$\times \int_0^{\infty} dz\, \frac{\cos(zq_{\parallel})}{(z^2 + b^2)^{3/2}} \int_0^{\sqrt{z^2+b^2}} dx\, x^2 g(x)\ , \qquad (18)$$

where q_T and $q_{\parallel}$ are, respectively, the perpendicular and parallel components of the momentum transfer relative to the incident beam direction. In the manner employed by Bemporad et al.[9], we calculate the Coulomb form factor in the three regions indicated in Fig. 23. The charge distribution is taken to be a uniform sphere with radius $R = [c^2 + (7/3)(\pi a)^2]^{1/2}$, where $c = 1.12A^{1/3}$ fm and $a = 0.545$ fm.[23] These terms correspond to parameters for an average radius given by the Woods-Saxon distribution,

$$g(r) = \frac{g_o}{1 + \exp(\frac{r-c}{a})} \tag{19}$$

Numerical integration was performed in each region as follows:

$$F_C^{int} = \frac{1}{q_\parallel R^3} \int_0^R db\, b^2\, e^{-\sigma'_\pi T(b)/2}\, e^{i\chi_C(b)}\, J_1(q_T b) \sin(q_\parallel \sqrt{R^2 - b^2})$$

$$F_C^{ext1} = q_\parallel \int_R^\infty db\, bK_1(q_\parallel b) J_1(q_T b) e^{i\chi_C(b)}$$

$$F_C^{ext2} = \int_0^R db\, b^2\, e^{-\sigma'_\pi T(b)/2}\, e^{i\chi_C(b)}\, J_1(q_T b) \int_{\sqrt{R^2-b^2}}^\infty dz\, \frac{\cos(q_\parallel z)}{(z^2 + b^2)^{3/2}} \,. \tag{20}$$

The amplitude for hadronic ρ production follows the form of Eq. (8), and for a point nucleus becomes $C_S^{1/2} q_T$. The Fourier transform of this amplitude is:

$$T_o(\vec{r}) = \frac{C_S^{\frac{1}{2}}}{(2\pi)^3} \int d^3q\, e^{-i\vec{q}\cdot\vec{r}} q_T$$

$$= \frac{iC_S^{\frac{1}{2}}}{(2\pi)^3} \hat{q}_T \cdot \vec{\nabla} \int d^3q\, e^{-i\vec{q}\cdot\vec{r}}$$

$$= \frac{iC_S^{\frac{1}{2}}}{(2\pi)^3} \hat{q}_T \cdot \vec{\nabla}\delta^3(\vec{r}) \,,$$

which indicates that strong production is proportional to the gradient of the nuclear density. Generalizing this result to the case of an extended nucleus we can write:[19]

$$f_S(q) = Ai \int d^3r\, e^{i\vec{q}\cdot\vec{r}}\, e^{-\sigma_\pi' T(b)/2}\, e^{i\chi_C(b)}\, \hat{q}_T \cdot \vec{\nabla} g(\vec{r}) \ . \tag{21}$$

Because this amplitude is more sensitive than the Coulomb amplitude to nuclear shape, we therefore used the Woods-Saxon distribution, given by Eq. (19), to characterize the nuclear shape in strong production. Substituting Eq. (19) into Eq. (21), we obtain:

$$f_S(q) = \frac{2\pi A g_o}{a} \int_{-\infty}^{\infty} dz\, e^{iq_\parallel z} \int_0^{\infty} db\, b^2\, J_1(q_T b)\, e^{-\sigma_\pi' T(b)/2}\, e^{i\chi_C(b)}$$

$$\times \frac{\exp\left(\dfrac{\sqrt{z^2+b^2}-c}{a}\right)}{\sqrt{z^2+b^2}\left[1+\exp\left(\dfrac{\sqrt{z^2+b^2}-c}{a}\right)\right]^2} \ . \tag{22}$$

Before comparing these calculations with the data, we took account of the resolution of the spectrometer. The observed cross section, $d\sigma/dt$, is a convolution of the true cross section, $d\sigma/d\tilde{t}$, with a resolution function, $R(\vec{q}_T, \vec{\tilde{q}}_T)$:

$$\frac{d\sigma}{dt} = \int d^2q_T\, R(\vec{q}_T, \vec{\tilde{q}}_T)\, \frac{d\sigma}{d\tilde{t}} \tag{23}$$

We assumed that the resolution function can be parameterized as a two-dimensional Gaussian in transverse momentum, that is:

$$R(\vec{q}_T, \vec{\tilde{q}}_T) = \frac{1}{2\pi\Delta^2} \exp\left[\frac{|\vec{q}_T - \vec{\tilde{q}}_T|^2}{-2\Delta^2}\right]$$

where $\vec{\tilde{q}}_T$ and $\vec{q}_T$ are the exact and the resolution-smeared transverse momenta, respectively.

The standard deviation, Δ , was determined from $K^- \to \pi^-\pi^o$ data, for which $\vec{\tilde{q}}_T = 0$. The Monte Carlo model for coherent ρ^- production indicated that the value of Δ at $\vec{\tilde{q}}_T$=0 was valid for finite $\vec{\tilde{q}}_T$ as well. In order to account for differences in multiple-Coulomb scattering in different targets, as well as for small topological differences between $K^- \to \pi^-\pi^o$ decays and ρ^- events, the value of Δ used in the analysis of any particular set of ρ^- data was obtained by extrapolating (via the Monte Carlo model) the Δ determined from the t-distribution of the corresponding $K^- \to \pi^-\pi^o$ data sample.

Folding in the resolution, the t-dependent factors $f_C(t)$ and $f_S(t)$ were calculated and averaged over t-intervals corresponding to the binning of the data. The three parameters, Γ_γ, C_S, and ϕ, were then varied to obtain the best fit of Eq. (12) to the data. We restricted the ranges of the fits, typically, to $t \lesssim 10(\hbar c)^2/R^2$ (first minimum in the optical model) to minimize the dependence of the results on details of the model, as well as to avoid regions of large t where there is more background and the resolution is less well known.

Table VI summarizes the results of the fits for the indicated ranges of t, and for the resolution-parameters shown in the table. In the global fits Γ_γ, C_S and ϕ were constrained to be the same for all nuclei. The errors on the extracted parameters are statistical. To check the stability of the solutions, we varied the ranges of t used in the fits; also, we performed fits including an incoherent background term of the form Dexp(-Et), where D and E are constants. In all cases the fits yielded acceptable χ^2 values,

and fluctuations in the values of the parameters for any target were within error. (For example, folding in systematic uncertainties in quadrature with statistical errors yielded a χ^2 of 5.5 for the deviation of the six individual measurements of Γ_γ at 156 GeV/c about their mean.) Fits were also performed using different values for the resolution (Δ). It was found that a 10% change in Δ produced a 4% change in the fitted value of Γ_γ.

In Table VII, we tabulate typical integrated values of $|T_C|^2$, $|T_S|^2$, and the interference term from Eq. (9), for $t < 0.005$ GeV^2. These values were calculated from numerical integrations over fitted curves. As an example of the shapes of these separate terms, we show in Fig. 24 the unsmeared Coulomb and strong-exchange cross sections for the Pb-2 target at 156 GeV/c.

V. CONCLUSIONS

Based on a weighted average of the fitted values for $\Gamma(\rho^- \to \pi^-\gamma)$ given in Table VI, and the checks of our normalization procedure, we quote the value 71 $\pm$ 7 KeV for the radiative width of the ρ^-. The major sources of uncertainty in this result are: normalization to K-decays ($\pm$4%), correction for the ρ-mass cut ($\pm$3%), and parameterization of the resolution function ($\pm$4%). The value for C_S is not well determined, but is consistent with extrapolations from measurements made at lower energies.[24] Our data are also not very sensitive to the relative phase ϕ.

Our result for $\Gamma(\rho^- \to \pi^-\gamma)$ is in good agreement with our previously reported value,[10] but is substantially higher than that of the earlier experimental measurement.[4] It is likely, however, that this discrepancy can be understood to result from the model used in the analysis of the previous experiment. At low energies, A_2 and π exchange can contribute to hadronic ρ production with an amplitude proportional to the neutron-proton excess.[25] In their calculations Gobbi et al.[4] assumed that only ω^o exchange

would contribute. Their fits showed a marked dependence on target material, and unless they constrained C_S to be the same for all targets, they could only determine a limit of 30 KeV to 80 KeV for $\Gamma(\rho \to \pi\gamma)$, a result consistent with ours. In our experiment we do not observe any obvious dependence of Γ on nuclear target. This is presumably because, at our energy, Coulomb production dominates over strong production. (That is, our data are insensitive to I=1 exchanges.)

Using our value for $\Gamma(\rho^- \to \pi^-\gamma)$ we obtain the ratio $\Gamma(\rho^- \to \pi^-\gamma)/\Gamma(\omega^o \to \pi^o\gamma)$ $= 0.090 \pm 0.013$, which is in reasonable agreement with the quark model prediction of 0.107. But, in fact, if we substitute the latest values for μ_u and μ_d, deduced from measurements of the proton and neutron magnetic moments,[13] into Eq. (4) we obtain a predicted ratio of 0.090, which is in even better agreement with our measurement. An overall fit to vector-meson radiative widths is also far more consistent with symmetry schemes when our value for $\Gamma(\rho^- \to \pi^-\gamma)$ is used in place of the older result.[26]

ACKNOWLEDGMENTS

We thank Drs. A. Brenner, A. Greene, J. Peoples, T. Toohig, A. Wehman and T. Yamanouchi of Fermilab for their support and interest in this experiment. We also wish to acknowledge the excellent assistance of the technical staffs at Fermilab, the Universities of Minnesota and Rochester in the design and construction of the equipment. Finally, we thank Dr. M. Zielinski for helpful discussions.

REFERENCES

1. S. Okubo, Phys. Letters 4, 14 (1963); S. L. Glashow, Phys. Rev. Letts. 11, 48 (1963); and K. Tanaka, Phys. Rev. 133, B1509 (1964) made the first predictions for radiative decay rates on the basis of SU(3) symmetry. Quark model calculations were introduced by C. Becchi and G. Morpurgo, Phys. Rev. 140B, 687 (1965); Y. Anisovitch et al., Phys. Letters 16, 194 (1965); W. Thirring, Phys. Letters 16, 335 (1965); L.Soloviev, Phys. Letters 16, 345 (1965). Also, see R. VanRoyan and V. F. Weisskopf, Nuovo Cimento A 50, 617 (1967) for a review of quark model calculations.

2. These assumptions are reviewed by N. Isgur, Phys. Rev. Letts. 36, 1262 (1976); T. Barnes, Phys. Letters 63B, 65 (1976); P. J. O'Donnel, Can. J. Physics 55, 1301 (1977), and Rev. Mod. Phys. 53, 673 (1981).

3. The value given for $\Gamma(\omega^{o} \to \pi^{o}\gamma)$ is an average of the three most recent experiments which directly measured the branching ratio $\Gamma(\omega^{o} \to \pi^{o}\gamma)/\Gamma(\omega^{o} \to \pi^{+}\pi^{-}\pi^{o})$: A. Baldin et al., Sov. J. Nucl. Physics 13, 431 (1971); D. Benaksas et al., Phys. Letters 42B, 511 (1972); J. Keyne et al., Phys. Rev. D14, 28 (1976). A discussion of this selection of experimental values is presented by T. Ohshima, Phys. Rev. D22, 707 (1980).

4. The result for $\Gamma(\rho^{-} \to \pi^{-}\gamma)$ was reported by B. Gobbi et al., Phys. Rev. Letts. 33, 1450 (1974); Phys. Rev. Letts. 37, 1439 (1976); L. Strawczynski, Ph.D. Thesis, University of Rochester report UR-475 (1974).

5. This method was originally proposed by H. Primakoff, Phys. Rev. 81, 899 (1951) to determine the lifetime of the π^{o}. The extension of this idea to radiative decays of mesons has been discussed by several authors: for example, M. L. Good and W. D. Walker, Phys. Rev. 120, 1855 (1960);

A. Halprin, C. M. Andersen, and H. Primakoff, Phys. Rev. 152, 1295 (1966); N. Jurisic and L. Stodolsky, Phys. Rev. D3, 724 (1971); M. Gourdin, Nucl. Physics B32, 415 (1971); G. Berlad et al., Ann. of Physics 75, 461 (1973).

6. See A. Halprin et al., or N. Jurisic and L. Stodolsky in Ref. 5.

7. K. Gottfried and J. D. Jackson, Nuovo Cimento 33, 309 (1964).

8. See, for example, L. Stodolsky, Phys. Rev. 144, 1145 (1966).

9. W. C. Carithers et al., Phys. Rev. Letts. 35, 349 (1975) have measured the radiative width of $\bar{K}^{*o}$ (890). C. Bemporad et al., Nucl. Physics B51, 1 (1973) have determined an upper limit for $\Gamma(K^{*+}(890) \rightarrow K^{+}\gamma)$. For results on ρ^{-} production see Ref. 4.

10. D. Berg et al., Phys. Rev. Letts. 44, 706 (1980).

11. Greater detail regarding the construction and operation of the apparatus may be found in T. Jensen, Ph.D. Thesis, University of Rochester Report UR-747 (1980).For a description of the LAC see C. Nelson et al,NIM, (to be published).

12. For a description of these charge-sensitive amplifiers see T. F. Droege, F. Lobkowicz, and Y. Fukushima, Fermilab Report TM-746 2500.000 (October, 1977).

13. Particle Data Tables, Rev. of Mod. Phys. 52, No. 2 (1980).

14. Yung-Su Tsai, Rev. of Mod. Phys. 46, 815 (1974).

15. J. C. Allaby et al., Sov. Journal of Nucl. Phys. 12, 295 (1971).

16. G. Fischer et al., Nucl. Phys. B16, 93 (1970).

17. P. Feller et al., Nucl. Phys. B104, 219 (1976).

18. H. Scott, Ph.D. Thesis, University of Rochester Report UR-529 (1975); J. Biel, Ph. D. Thesis, University of Rochester Report UR-614 (1976); J. Biel et al., Phys. Rev. D18, 3079 (1978); Phys. Rev. D20, 33 (1979).

19. G. Fäldt et al., Nucl. Phys. B41, 125 (1972); Nucl. Phys. B43, 591 See also the papers referred to in Refs. 4 and 9.

20. J. D. Jackson, Nuovo Cimento 34, 1644 (1964).

21. We have recently completed a high-statistics data run with positive beam from which we should be able to obtain a more accurate parameterization of the ρ line shape.

22. We have used the values, $\alpha = 0.015$ at 156 GeV/c and $\alpha = 0.10$ at 260 GeV/c, given by J. Burq et al., CERN EP Internal Report 78-07 (1978). The π-nucleon cross section, $\sigma_{\pi} = 24.5$ mb, was obtained from the Particle Data Tables (Reference 13).

23. B. Hahn, D. G. Ravenhall and R. Hofstadter, Phys. Rev. 101, 1131 (1956). H. R. Collard, L. R. B. Elton, and R. Hofstadter, Nuclear Radii, edited by H. Schopper, Landolt-Bornstein, Numerical Data and Functional Relationships in Science and Technology, New Series, (Springer-Verlag, Berlin, 1967), Group I, Vol. 2.

24. For ω° exchange, C_S is expected to scale at $1/p_{lab}$. D. J. Crennel et al., Phys. Rev. Letts. 27, 1674 (1971), report $C_S = 13.7 \pm 2.2$ mb/GeV^4 at 6 GeV/c; J. Bartsch et al., Nucl. Phys. B46, 46 (1972), report $C_S = 6.9 \pm 1.5$ mb/GeV^4 at 16 GeV/c; B. Gobbi et al., Ref. 4, report $C_S = 4.0 \pm 1.0$ mb/GeV^4 at 22.7 GeV/c.

25. A. N. Kamal and G. L. Kane, Phys. Rev. Letts. 43, 551 (1979).

26. P. J. O'Donnell in Ref. 2; T. Ohshima in Ref. 3; B. J. Edwards and A. N. Kamal, SLAC-PUB-2303 (1979); D. A. Geffen and Warren Wilson, Phys. Rev. Letts. 44, 370 (1980).

Table I. Properties of the Targets

Element	Atomic Number	Atomic Weight	Thickness[a] (cm) ±0.003	(gm/cm^2)	Number of radiation lengths	Number of collision lengths[b]	$A/N_o \rho t$ (Barns)
Carbon (C)	6	12.01	2.540	4.52 ±0.03	0.106	0.0770	4.41 ± 0.03
Aluminum (Al)	13	26.98	0.952	2.643 ±0.007	0.110	0.0384	16.95 ± 0.04
Copper (Cu-1)	29	63.54	0.157	1.396 ±0.004	0.109	0.0168	75.58 ± 0.21
Copper (Cu-2)	29	63.54	0.318	2.827 ±0.007	0.220	0.0340	37.32 ± 0.10
Lead (Pb-1)	82	207.19	0.079	0.873 ±0.005	0.137	0.0078	394.1 ± 2.2
Lead (Pb-2)	82	207.19	0.160	1.768 ±0.008	0.278	0.0158	194.6 ± 1.0

(a) Area: 2.10 cm × 2.10 cm

(b) For nucleons

Table II. Correction Factors for Beam Flux

Particle type	Beam Momentum (GeV/c) -156	+156	-260
K	1.03 ± 0.01	1.03 ± 0.01	1.03 ± 0.01
P	1.04 ± 0.015	1.017 ± 0.005	1.06 ± 0.02
π	1.025 ± 0.007	1.027 ± 0.007	1.029 ± 0.007

Table III. Target-Dependent Correction Factors

Target	δ-ray veto[a]	Absorption of photons from a π°	Charged-track absorption[b] π	K	P
C	1.063 ± 0.02	1.086 ± 0.008	1.042	1.038	1.062
Al	1.043 ± 0.02	1.089 ± 0.003	1.020	1.018	1.028
Cu-1	1.026 ± 0.02	1.088 ± 0.003	1.008	1.008	1.011
Cu-2	1.043 ± 0.005	1.187 ± 0.003	1.017	1.016	1.022
Pb-1	1.015 ± 0.02	1.112 ± 0.006	1.004	1.004	1.005
Pb-2	1.026 ± 0.02	1.241 ± 0.006	1.008	1.007	1.009

(a) This was measured only for Cu-2 and extrapolated to other targets, assuming that the effect scaled with target thickness in gm/cm^2.

(b) Errors are somewhat smaller than those in column 3.

Table IV. Corrections Related to the Design of the Spectrometer

Spectrometer-Related Correction	Correction Factor
a) Absorption in the S-counter (0.21 ± 0.02 gm/cm^2 of polystyrene)	
pion absorption	1.002 ± 0.0004
kaon absorption	1.002 ± 0.0004
proton absorption	1.003 ± 0.0006
absorption of photons from π^o decay	1.008 ± 0.0010
b) Material in the chambers, counters, etc. amounted to $2.3 \pm 0.2 \times 10^{-2}$ proton-collision lengths and $6.9 \pm 0.4 \times 10^{-2}$ radiation lengths.	
pion absorption	1.015 ± 0.003
kaon absorption	1.014 ± 0.003
proton absorption	1.024 ± 0.003
absorption of photons from π^o decay	1.114 ± 0.005
c) Losses caused by random firing of any of the counters V1-V4, H, A1, A2, AM, and the U/D counters.	1.010 ± 0.003
d) Correction due to an upper-level discriminator threshold that was applied to the S-counter signal. This correction, for losses of triggers with large pulse heights (high-energy tail of the Landau energy-loss distribution), was estimated from a pulse-height spectrum obtained with the upper-threshold requirement removed from the trigger.	1.027 ± 0.005

Table V. Correction factors applied in determining the cross section for the process $\pi^- A \to A\pi^-\pi^o$

Energy (GeV/c)	-156						-260	
Target	C	Al	Cu-1	Cu-2	Pb-1	Pb-2	Cu-2	Pb-1
Corrections common to K-decay	1.393	1.373	1.351	1.373	1.330	1.344	1.318	1.296
Beam-count correction	1.025±0.007						1.029 ± 0.007	
Absorption in S-Counter	1.009 ± 0.001							
Absorption in target	1.132±0.010	1.11±0.004	1.097±0.003	1.207±0.004	1.116±0.007	1.251±0.007	1.207±0.004	1.256±0.007
Rho-mass cut	1.13 ± 0.03							
Geometric acceptance[(a)]	2.11 ± 0.05						2.06 ±0.06	1.81 ±0.05
K-decay normalization	1.21 ±0.05	1.21±0.05	1.13 ±0.04	1.21 ±0.04	1.13 ±0.05	1.15 ±0.04	1.14 ±0.11	1.01 ±0.05
Total C.F.	4.73 ±0.31	4.54±0.30	4.14 ±0.25	4.94 ±0.30	4.16 ±0.27	4.79 ±0.29	4.41 ±0.53	3.50 ±0.25
σ (per event) (μb/event)[(b)]	0.048±0.003	0.298±0.019	0.732±0.044	0.639 ±0.038	6.78 ±0.44	1.393 ±.084	1.41 ±0.17	1.51 ±0.11

(a) Averaged over the mass interval 0.55 GeV < $M_{\pi^-\pi^o}$ < 0.95 GeV, using a $\sin^2\theta\sin^2\phi$ distribution for the decay of the ρ^-.

(b) Errors include uncertainties in the target thicknesses, as well as in the correction factors.

Table VI. Results of Parameterization of Data (all quoted errors are statistical)

Target	t-range (GeV^2)	Δ (MeV)	Γ_γ (KeV)	$C_S\left(\frac{mb}{GeV^4}\right)$	ϕ (degrees)	χ^2/d.o.f.
			156 GeV/c			
C	<0.05	9.6	77.5 ± 7.8	0.9 ± 0.2	68 ± 20	13.8/9
Al	<0.03	10.2	88.2 ± 10.0	0.9 ± 0.2	29 ± 34	5.2/7
Cu-1	<0.015	9.8	61.3 ± 5.4	1.0 ± 0.3	-23 ± 46	11.8/7
CU-2	<0.01	11.0	75.9 ± 5.5	0.6 ± 0.5	-19 ± 60	5.9/6
Pb-1	<0.01	10.3	68.0 ± 8.3	0.6 ± 0.5	65 ± 50	0.9/4
Pb-2	<0.01	11.5	78.7 ± 4.0	0.7 ± 0.2	60 ± 23	11.7/9
Global[(a)]	<0.01	-	73.4 ± 2.5	0.6 ± 0.1	24 ± 18	59.5/47
			260 GeV/c			
Cu-2	<0.01	11.2	74.5 ± 8.0	0.5 ± 0.7	-57 ± 105	1.8/5
Pb-2	<0.01	11.9	60.5 ± 4.1	2.9 ± 1.0	-72 ± 20	12.2/13
Global[(a)]	<0.01	-	68.5 ± 3.1	0.6 ± 0.2	14 ± 10	23.4/21

(a) Fit to all data at each energy, constraining Γ_γ, C_S and ϕ to be independent of nuclear material.

Table VII. Integrated Cross Sections for Coherent ρ Production on Nuclei

	Target	$\int_0^{.005} dt\|T_C\|^2$ (μb)	$\int_0^{.005} dt\|T_S\|^2$ (μb)	$2Re \int_0^{.005} dt\, T_C^* T_S e^{i\phi}$ (μb)
-156	C	6.9 ± 0.9	0.9 ± 0.3	0.7 ± 0.4
GeV/c	Al	35.7 ± 4.6	3 ± 1	8 ± 5
	Cu-1	113 ± 12	11 ± 4	30 ± 30
	CU-2	139 ± 14	7 ± 7	25 ± 25
	Pb-1	906 ± 128	24 ± 16	51 ± 49
	Pb-2	1057 ± 81	20 ± 8	25 ± 40
-260	Cu-2	173 ± 28	6 ± 7	17 ± 15
GeV/c	Pb-2	993 ± 116	117 ± 56	142 ± 100

FIGURE CAPTIONS

Fig. 1 a) Diagram for Primakoff production in the Coulomb field of a nucleus of charge Z. b) Gottfried-Jackson reference frame for the coherent process $\pi^- A \to A\pi^-\pi^o$.

Fig. 2 Schematic diagram of the spectrometer.

Fig. 3 Schematic diagram for the assembly of the liquid argon calorimeter.

Fig. 4 Studies of the response of the LAC to Bremsstrahlung electrons. a) Energy resolution of the LAC (standard deviation squared) as a function of electron momentum. The dashed line corresponds to a resolution function of the form $\sigma_E^2 = 0.18 + (0.20)^2 E\ (GeV^2)$. b) Plot of the difference between the X-position of the electron as measured by the drift chambers and as measured by the LAC.

Fig. 5 Schematic of the arrangement of scintillation counters used in the trigger.

Fig. 6 Distributions of two-photon masses for K-decay events at 156 GeV/c and 260 GeV/c. The arrows indicate the limits used to define π^o's. The smooth curves are predictions of the Monte Carlo normalized to the total number of events in the distributions.

Fig. 7 Distributions in the total energy of $\pi^-\pi^o$ systems resulting from K^- decays. The arrows indicate the limits used to define $K^- \to \pi^-\pi^o$ events. The smooth curves are Monte Carlo predictions normalized to the number of events between the arrows.

Fig. 8 Decay-vertex distributions for $K^- \to \pi^-\pi^o$ events at 156 GeV/c and 260 GeV/c. The arrows indicate the data sample chosen for studies of resolution and normalization. The smooth curves are predictions of the Monte Carlo normalized to the number of events between the arrows.

Fig. 9 Distributions in the $\pi^-\pi^o$ mass for $K^- \to \pi^-\pi^o$ decays at 156 GeV/c and 260 GeV/c. The smooth curves are predictions of the Monte Carlo normalized to the total number of events in the distributions. The arrows indicate the limits used to define the $K^- \to \pi^-\pi^o$ signal.

Fig. 10 Distributions in the square of the transverse distance of the π^- from beam center for $K^- \to \pi^-\pi^o$ decays at the position of the D1 chamber for 156 GeV/c and 260 GeV/c. The smooth curves are predictions of the Monte Carlo.

Fig. 11 Distributions in the energy asymmetry for the two photons from π^o decays resulting from $K^- \to \pi^-\pi^o$ decays at 156 GeV/c and 260 GeV/c. The smooth curves are predictions of the Monte Carlo.

Fig. 12 Decay-angle distributions in the helicity frame for the process $K^- \to \pi^-\pi^o$ at 156 GeV/c and 260 GeV/c. The smooth curves are predictions of the Monte Carlo assuming an isotropic decay of the K^-.

Fig. 13 t-distributions for $K^- \to \pi^-\pi^o$ events accumulated with a lead target at 156 GeV/c and 260 GeV/c, and no target in place at 156 GeV/c.

Fig. 14 Sample of Ke3 events accumulated at 156 GeV/c. a) Decay-vertex distribution. b) Electron momentum spectrum for those events with a decay vertex between the arrows indicated in a). The smooth curves are predictions of the Monte Carlo.

Fig. 15 Plot of the measured yield divided by expected yield for $K^- \to \pi^-\pi^o$ events for different targets and both incident energies. (Points for which no target was present are indicated by the symbol MT.)

Fig. 16 a) Cross section for the process $p + Pb \to Pb + p\pi^o$ for $t < 0.001$ GeV^2 as a function of $M_{p\pi^o}$. The solid curve is the prediction for Coulomb production of $\Delta^+(1232)$ based on measurements for the process $\gamma p \to p\pi^o$. b) Mass-dependent acceptance of the spectrometer for the process $\Delta^+ \to p\pi^o$. c) Decay-angle distribution in the Gottfried-Jackson frame for $p\pi^o$ events produced on lead at

$t < 0.001$ GeV^2 with 1.14 GeV $< M_{p\pi^0} <$ 1.28 GeV. The smooth curve is the prediction of the Monte Carlo assuming a $1 + 3\sin^2\theta\sin^2\phi$ distribution for $\Delta^+(1232)$ decay.

Fig. 17 Interaction-vertex distributions for the process $\pi^- Pb \to Pb\pi^-\pi^0$ at 156 GeV/c and 260 GeV/c. The smooth curves are predictions of the Monte Carlo normalized to the total number of events in the distributions. The limits indicated by the arrows were used to define interactions in the target.

Fig. 18 $\pi^-\pi^0$ mass distributions for the coherent process $\pi^- A \to A\pi^-\pi^0$ for the different targets at the two energies. The arrows indicate the limits used to define ρ^- production.

Fig. 19 Total energy for the process $\pi^- A \to A\pi^-\pi^0$ on a) carbon, b) copper, and c) lead at 156 GeV/c. The shaded regions correspond to events at $t < 0.002$ GeV^2. The arrows indicate the cuts applied to define the coherent $\pi^-\pi^0$ signal.

Fig. 20 a), b) Acceptance-corrected distributions of the decay angle in the Gottfried-Jackson frame for the process $\pi^- Pb \to Pb\pi^-\pi^0$ at 156 GeV/c and 260 GeV/c. The dashed lines indicate the $\sin^2\theta$ shape expected for decays of coherently produced ρ^- mesons. c) Distribution in the Gottfried-Jackson angle ϕ for the coherent process $\pi^- C \to C\pi^-\pi^0$ at 156 GeV/c. The smooth curve is the Monte Carlo prediction, based on a $\sin^2\theta\sin^2\phi$ decay of the ρ^- and a t-distribution similar to that observed in the carbon data.

Fig. 21 t-distributions for the process $\pi^- A \to A\rho^-$ for the different targets at the two energies. The curves are fits to the data used for extracting the parameters listed in Table VI.

Fig. 22 Acceptance-corrected $\pi^-\pi^0$ mass spectra for the process $\pi^- Pb \to Pb\pi^-\pi^0$ at small t at 156 GeV/c (a), and 260 GeV/c (b). The acceptance is indicated by the curves above the data. The smooth curves through the data points are fits assuming the Breit-Wigner shape described in the text.

Fig. 23 Definition of the regions over which the electromagnetic form factor is calculated.

Fig. 24 Relative contributions from the Coulomb and strong terms in coherent ρ^- production at 156 GeV/c on lead, prior to the introduction of resolution smearing.

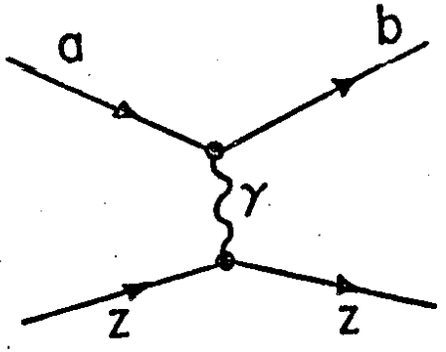
a
b
γ
z
z

(a)

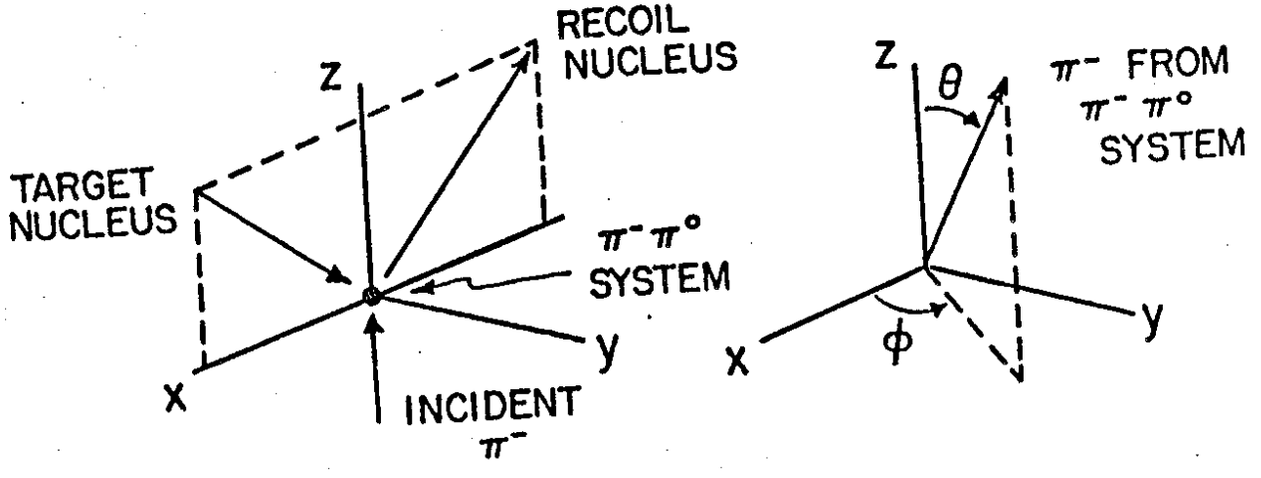
RECOIL
NUCLEUS
z
TARGET
NUCLEUS
π⁻π°
SYSTEM
y
x
INCIDENT
π⁻
z
θ
π⁻ FROM
π⁻π°
SYSTEM
x
φ
y

(b)

Fig 1

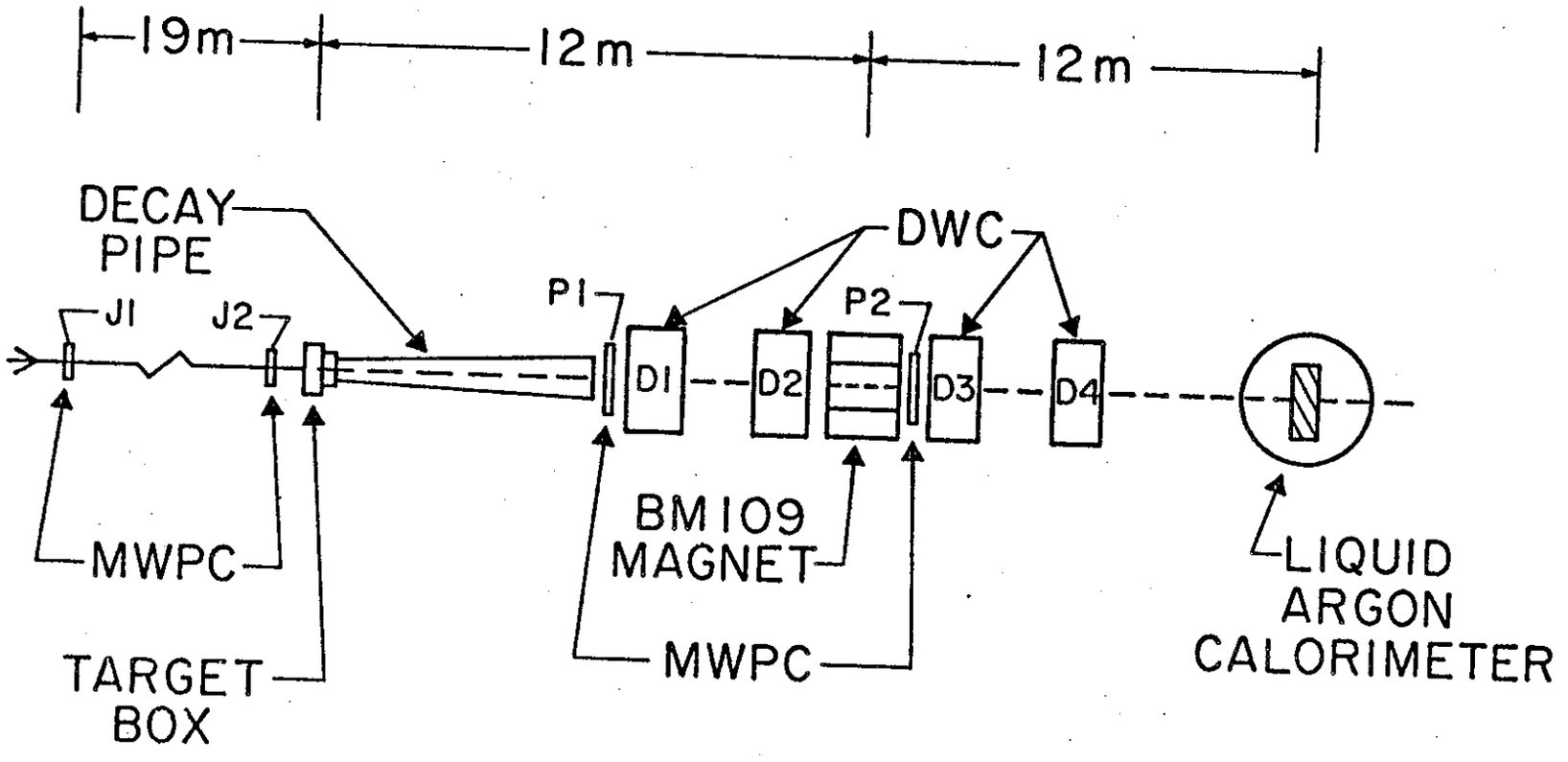
19m
12m
12m
DECAY
PIPE
J1
J2
P1
P2
DWC
D1
D2
D3
D4
MWPC
TARGET
BOX
BM109
MAGNET
MWPC
LIQUID
ARGON
CALORIMETER

Fig 2

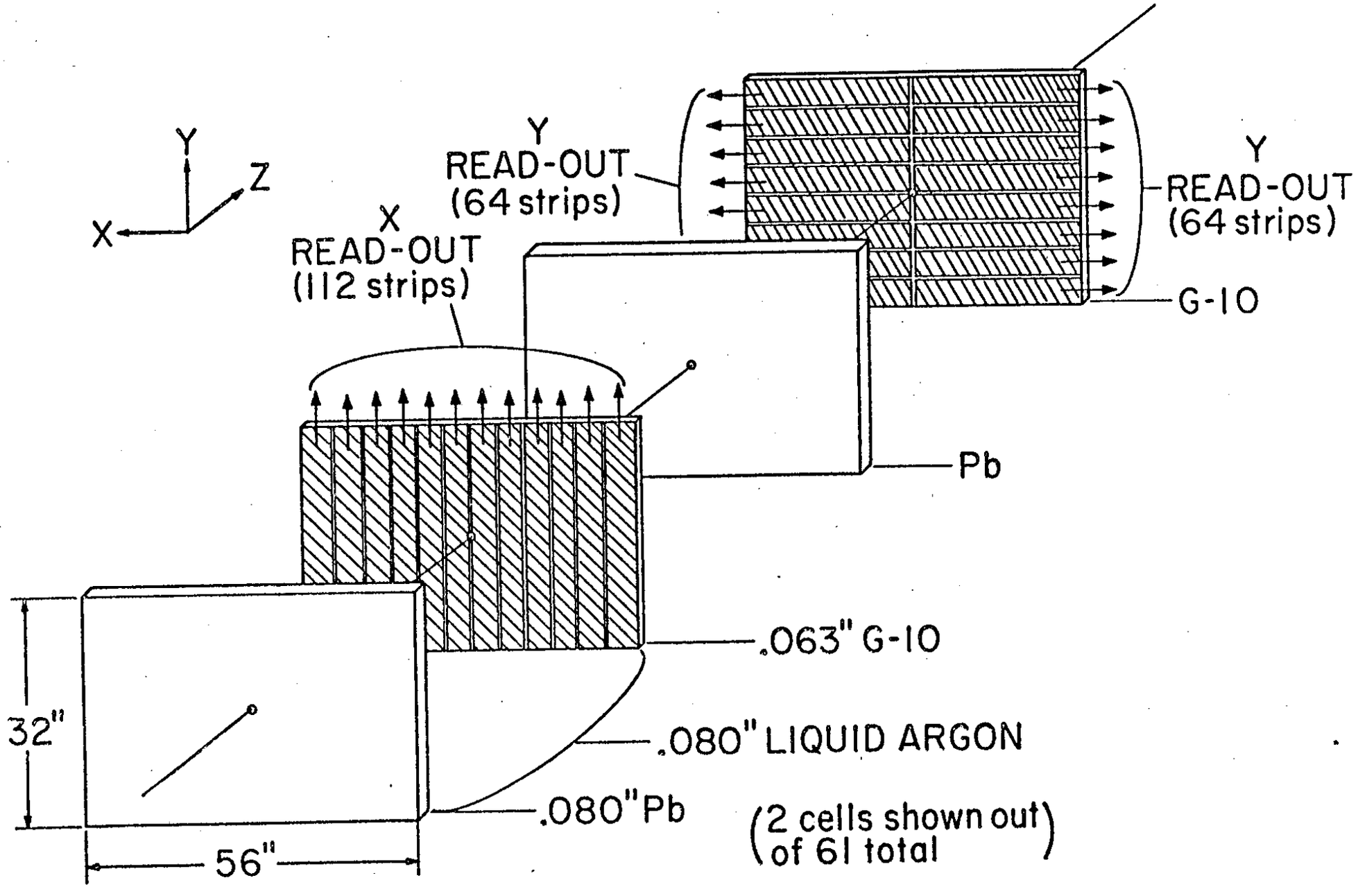
Y
Z
X
Y
READ-OUT
(64 strips)
X
READ-OUT
(112 strips)
Y
READ-OUT
(64 strips)
G-10
Pb
.063" G-10
.080" LIQUID ARGON
.080" Pb
32"
56"
(2 cells shown out
of 61 total

Fig 3

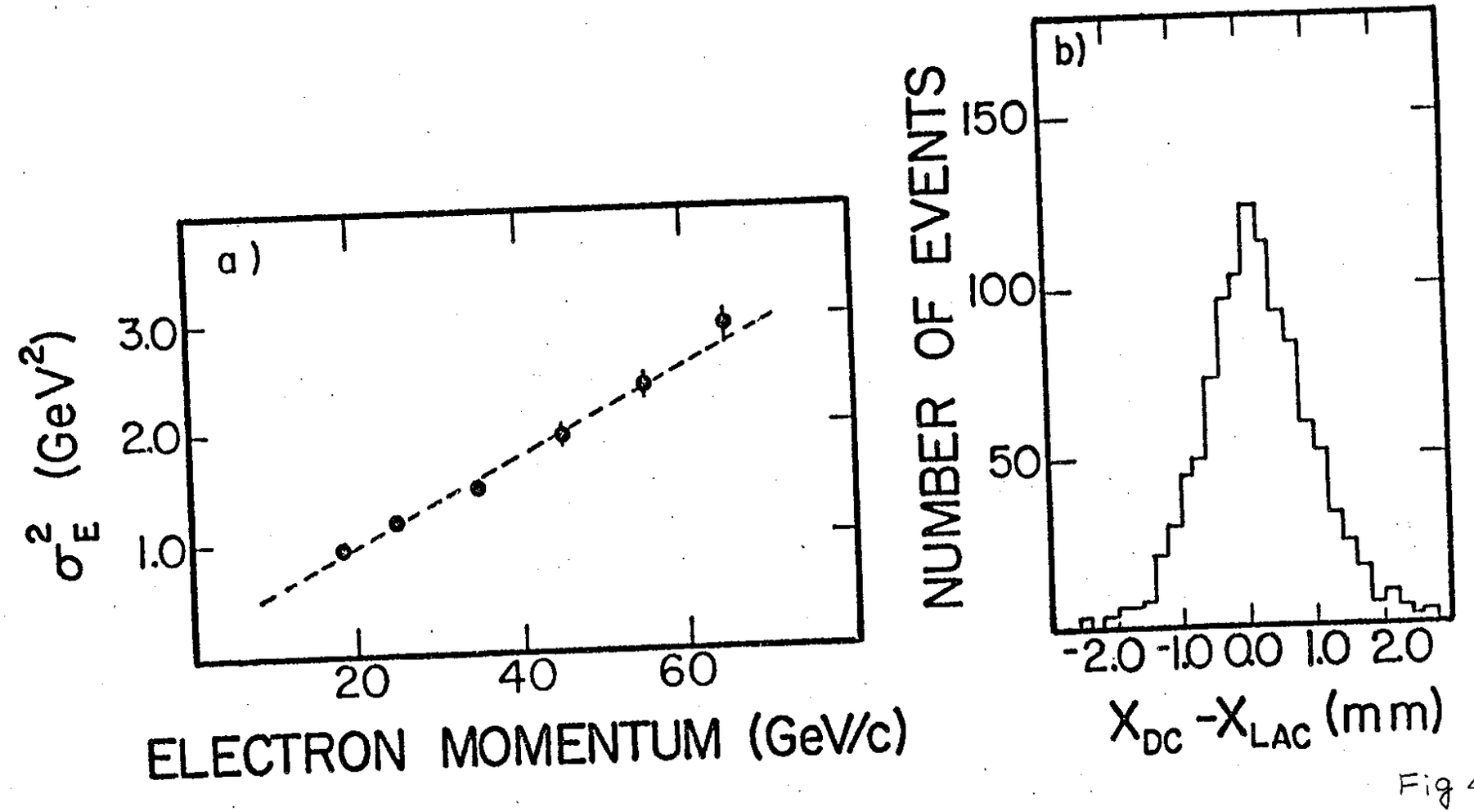
a)
σ_E^2 (GeV^2)
3.0
2.0
1.0
20
40
60
ELECTRON MOMENTUM (GeV/c)
b)
NUMBER OF EVENTS
150
100
50
-2.0 -1.0 0.0 1.0 2.0
$X_{DC} - X_{LAC}$ (mm)

Fig 4

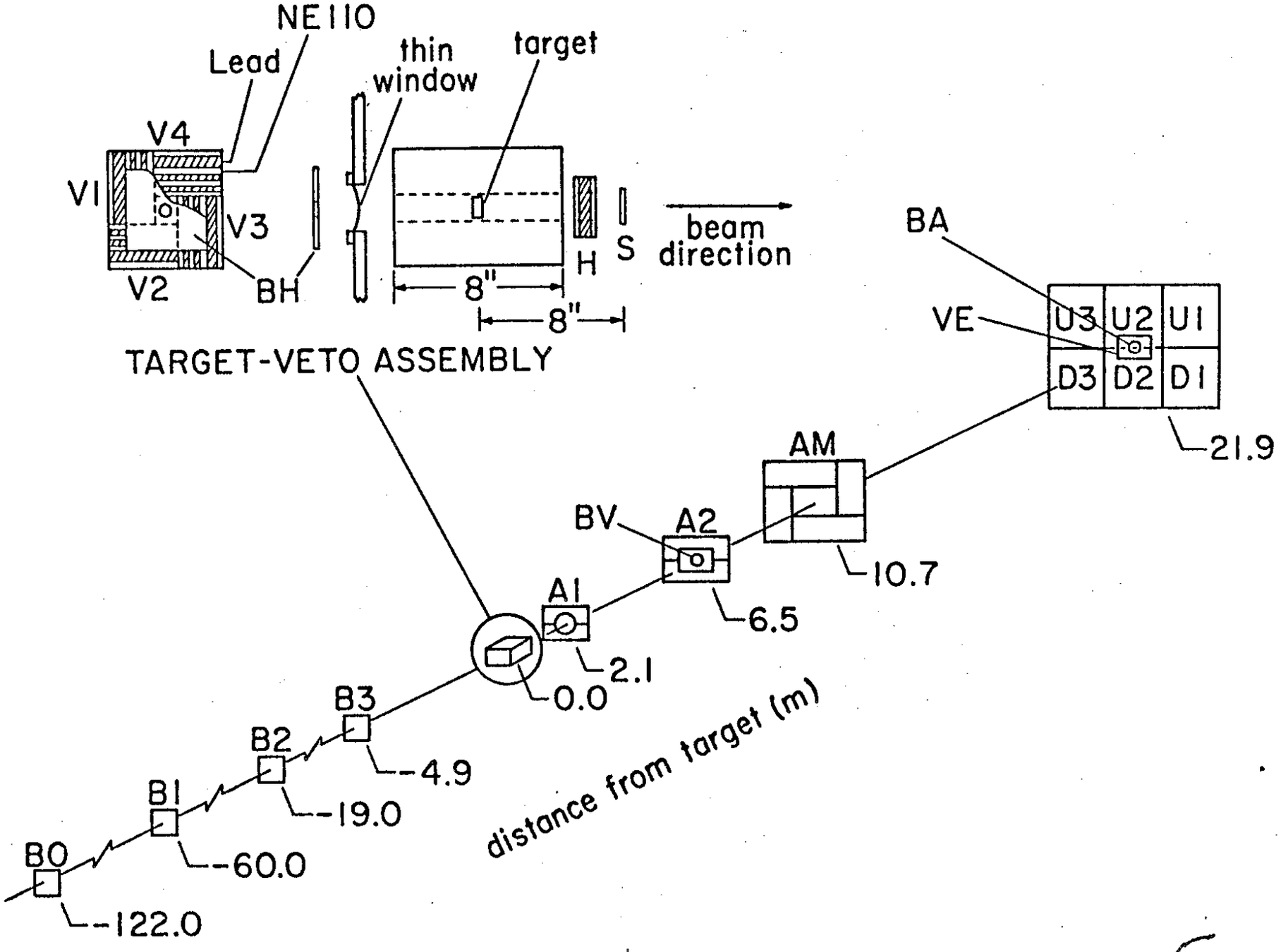
NE110
Lead
thin window
target
V4
V1
V3
V2
BH
H
S
8"
8"
beam direction
TARGET-VETO ASSEMBLY
BA
VE
U3
U2
U1
D3
D2
D1
21.9
AM
BV
A2
10.7
6.5
A1
2.1
0.0
B3
B2
B1
B0
4.9
19.0
60.0
122.0
distance from target (m)

Fig 5

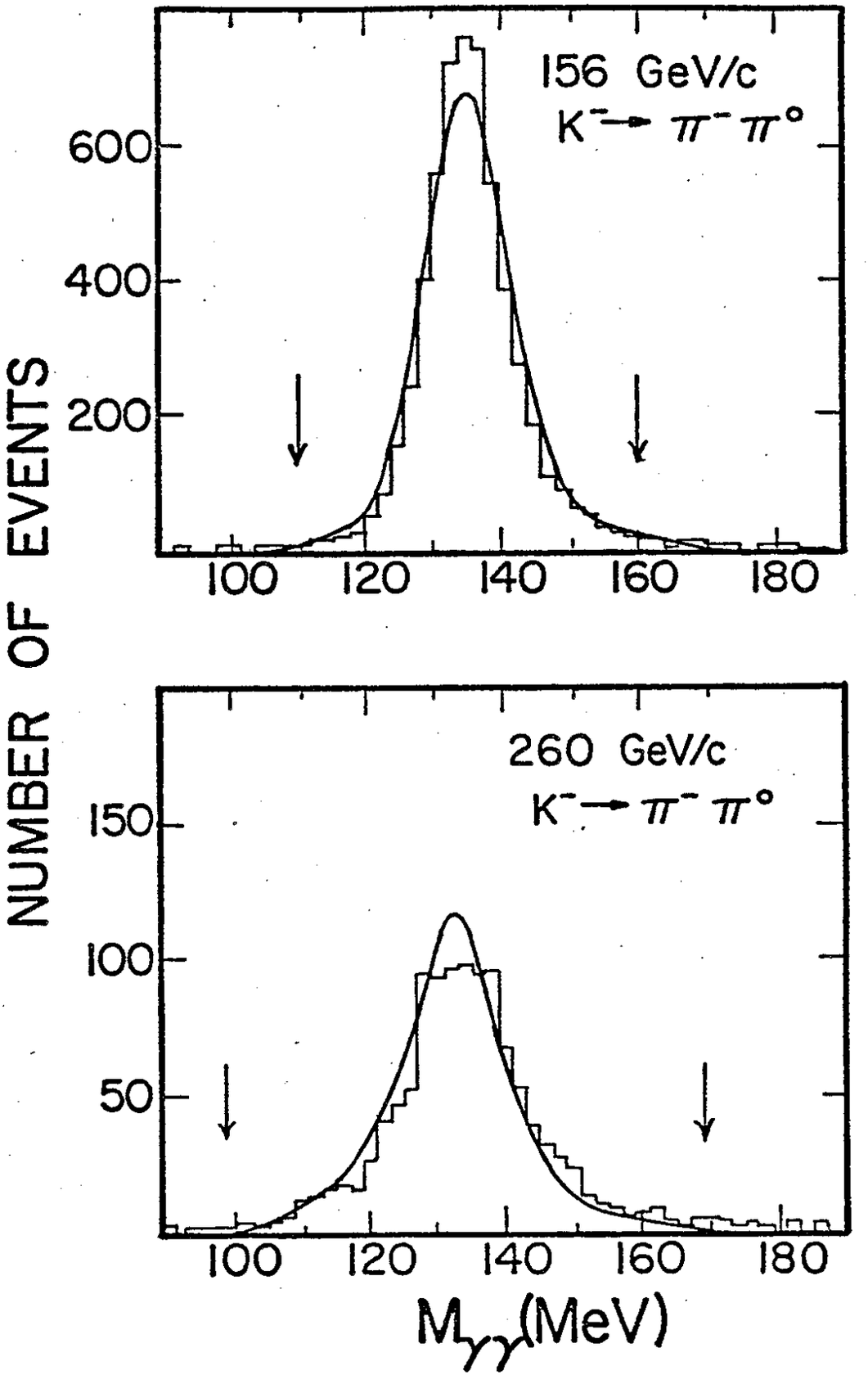
156 GeV/c
K⁻ → π⁻ π°
600
400
200
100
120
140
160
180
NUMBER OF EVENTS
260 GeV/c
K⁻ → π⁻ π°
150
100
50
100
120
140
160
180
Mγγ(MeV)

Fig 6

Fig

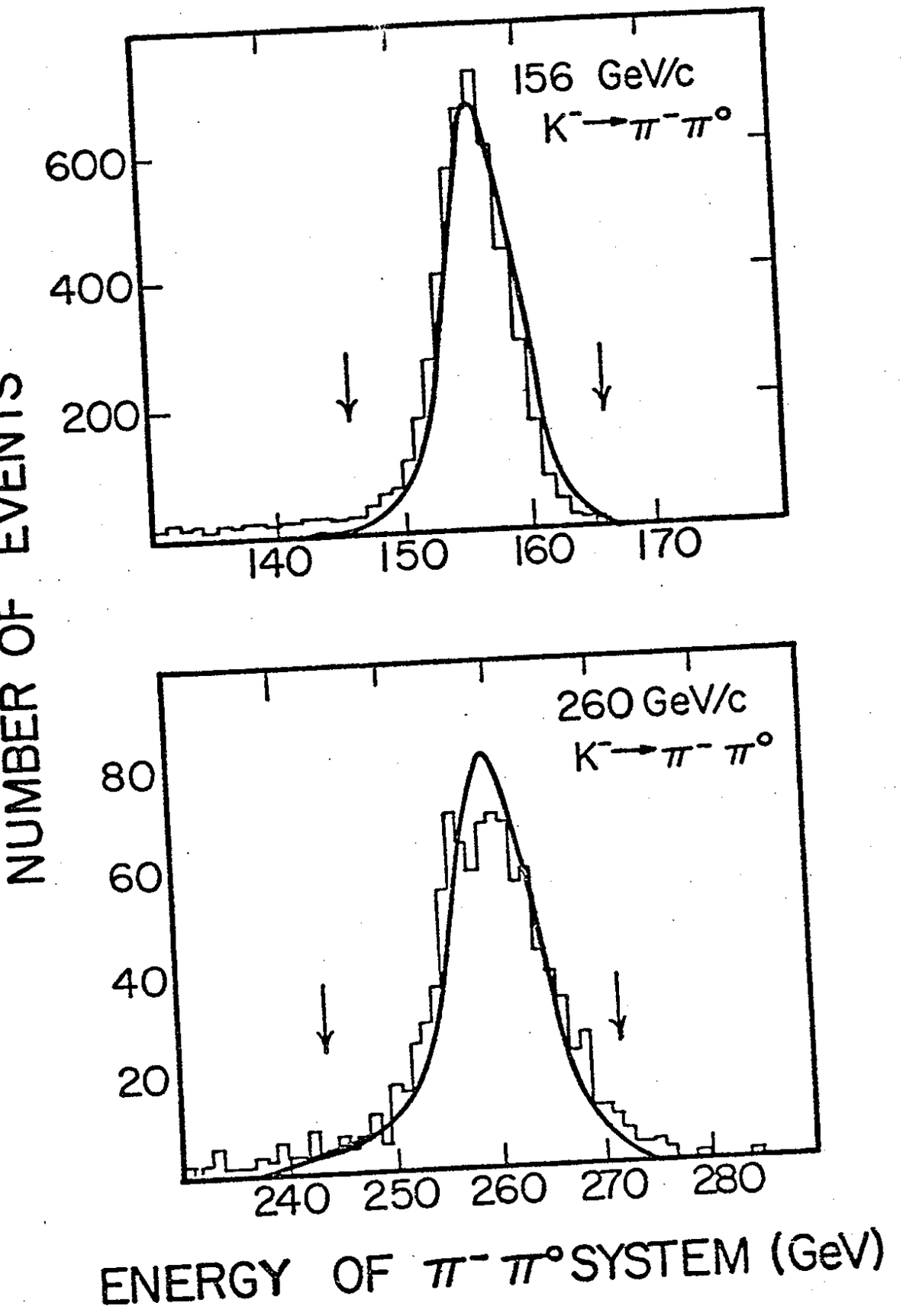
156 GeV/c
K⁻ → π⁻ π°
600
400
200
140
150
160
170
260 GeV/c
K⁻ → π⁻ π°
80
60
40
20
240
250
260
270
280
NUMBER OF EVENTS
ENERGY OF π⁻ π° SYSTEM (GeV)

Fig 7

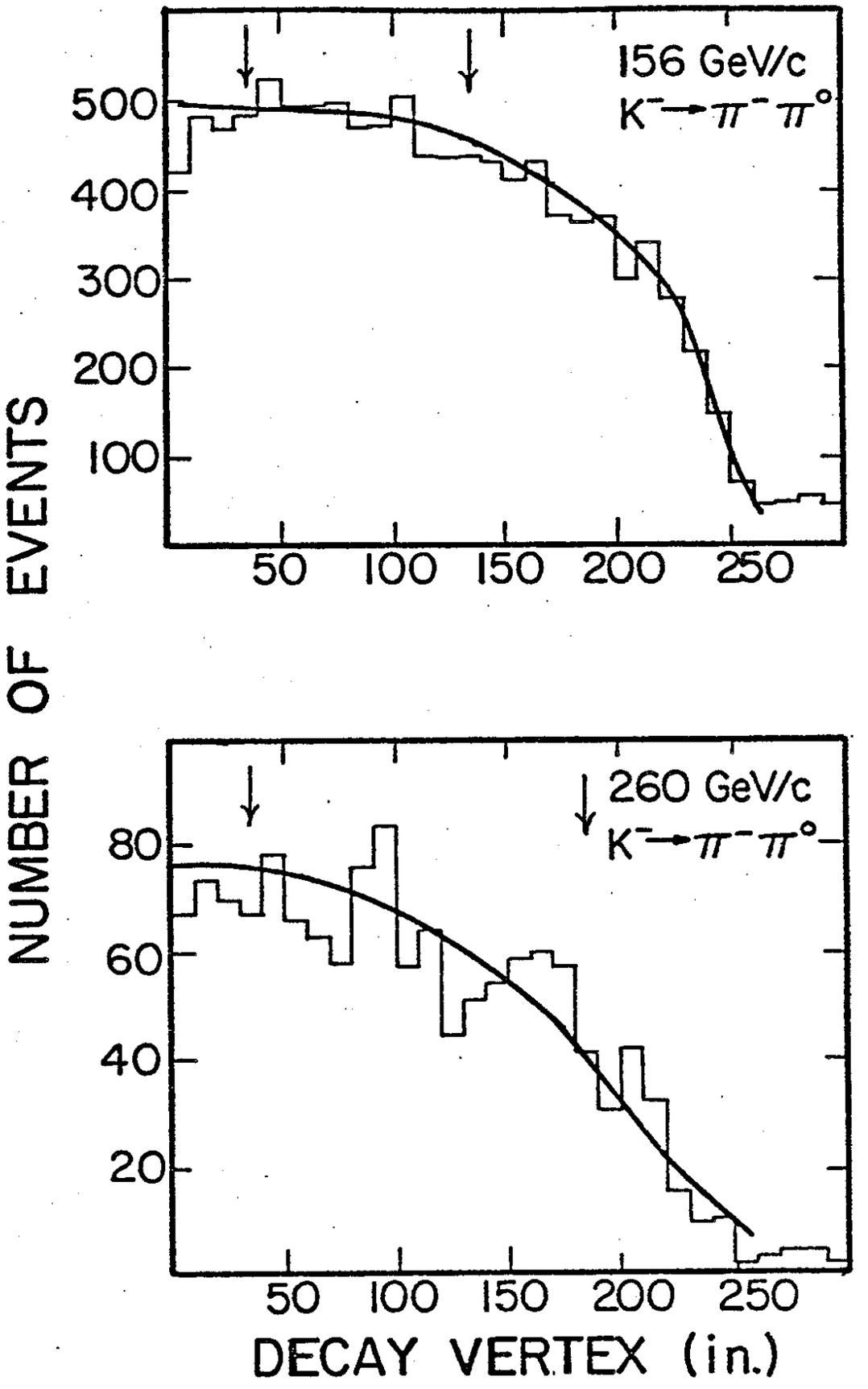
156 GeV/c
K⁻→π⁻π°
500
400
300
200
100
50
100
150
200
250
260 GeV/c
K⁻→π⁻π°
80
60
40
20
50
100
150
200
250
NUMBER OF EVENTS
DECAY VERTEX (in.)

Fig 8 Fig

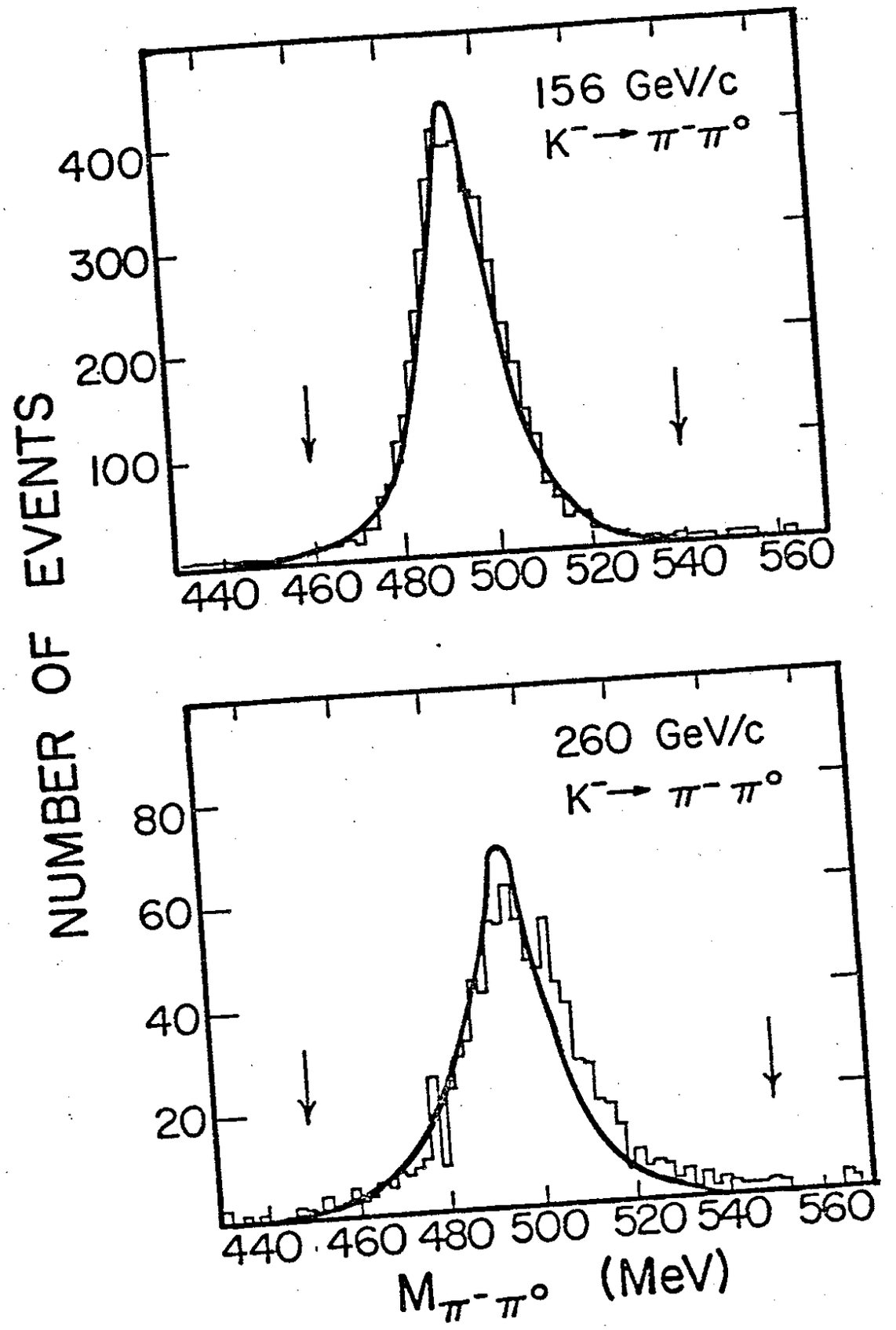
156 GeV/c
K⁻ → π⁻π°
400
300
200
100
260 GeV/c
K⁻ → π⁻π°
80
60
40
20
NUMBER OF EVENTS
440 460 480 500 520 540 560
440 460 480 500 520 540 560
Mπ⁻π° (MeV)

Fig 9

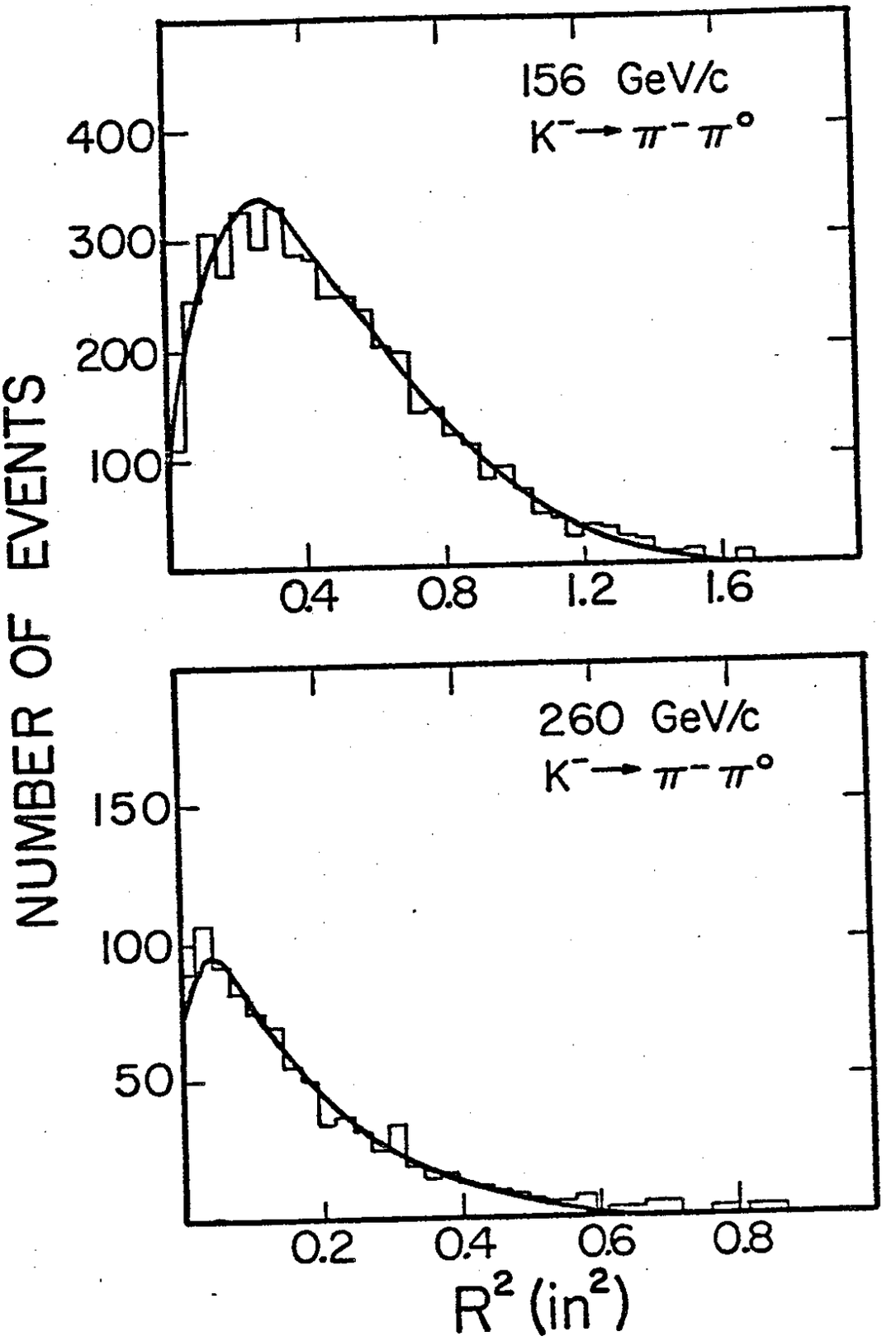
156 GeV/c
K⁻ → π⁻ π°
400
300
200
100
0.4
0.8
1.2
1.6
260 GeV/c
K⁻ → π⁻ π°
150
100
50
0.2
0.4
0.6
0.8
NUMBER OF EVENTS
R² (in²)

Fig 10

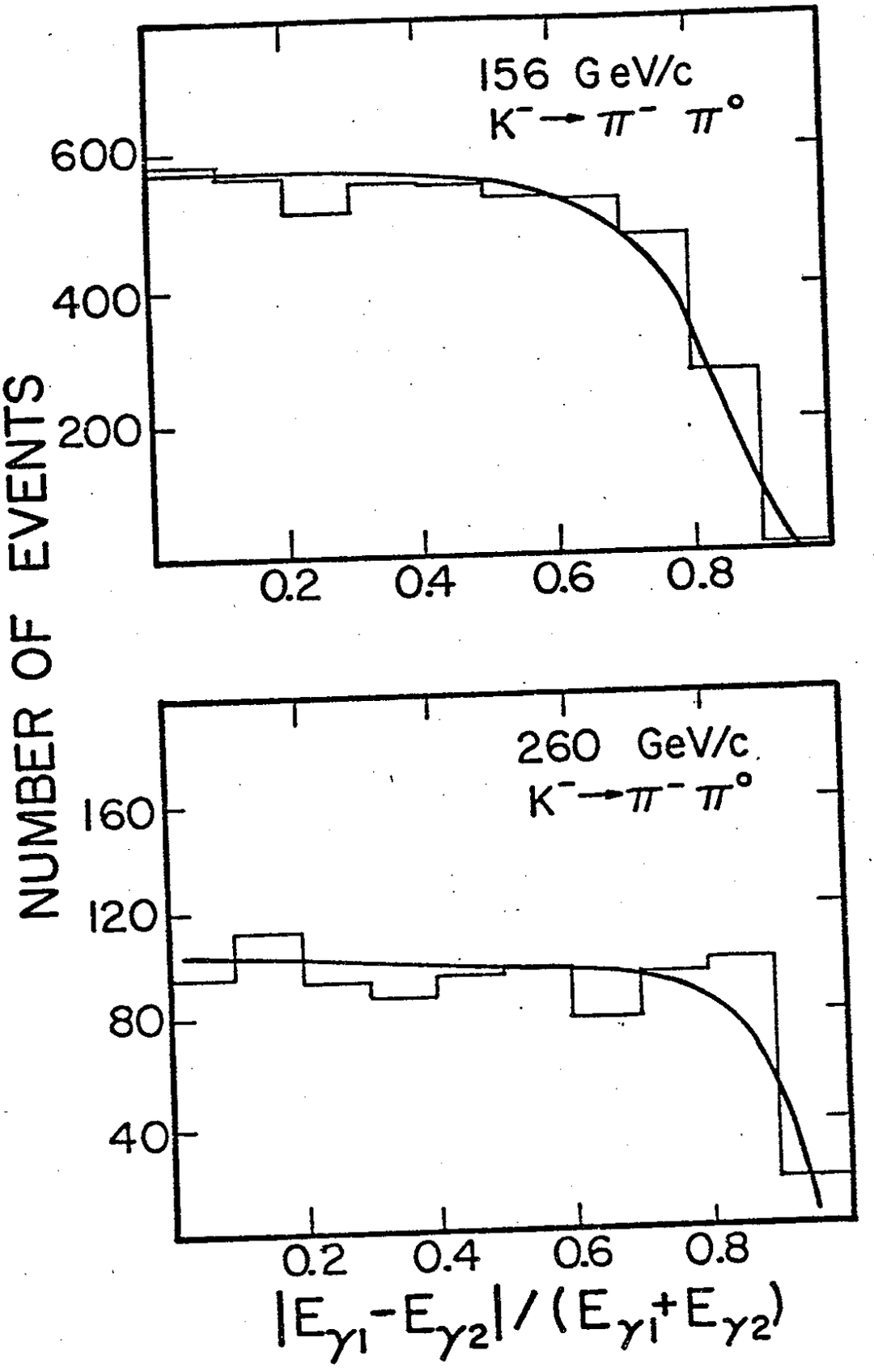
156 GeV/c
K⁻ → π⁻ π°
600
400
200
0.2
0.4
0.6
0.8
260 GeV/c
K⁻ → π⁻ π°
160
120
80
40
0.2
0.4
0.6
0.8
NUMBER OF EVENTS
|Eγ1 - Eγ2| / (Eγ1 + Eγ2)

Fig 11

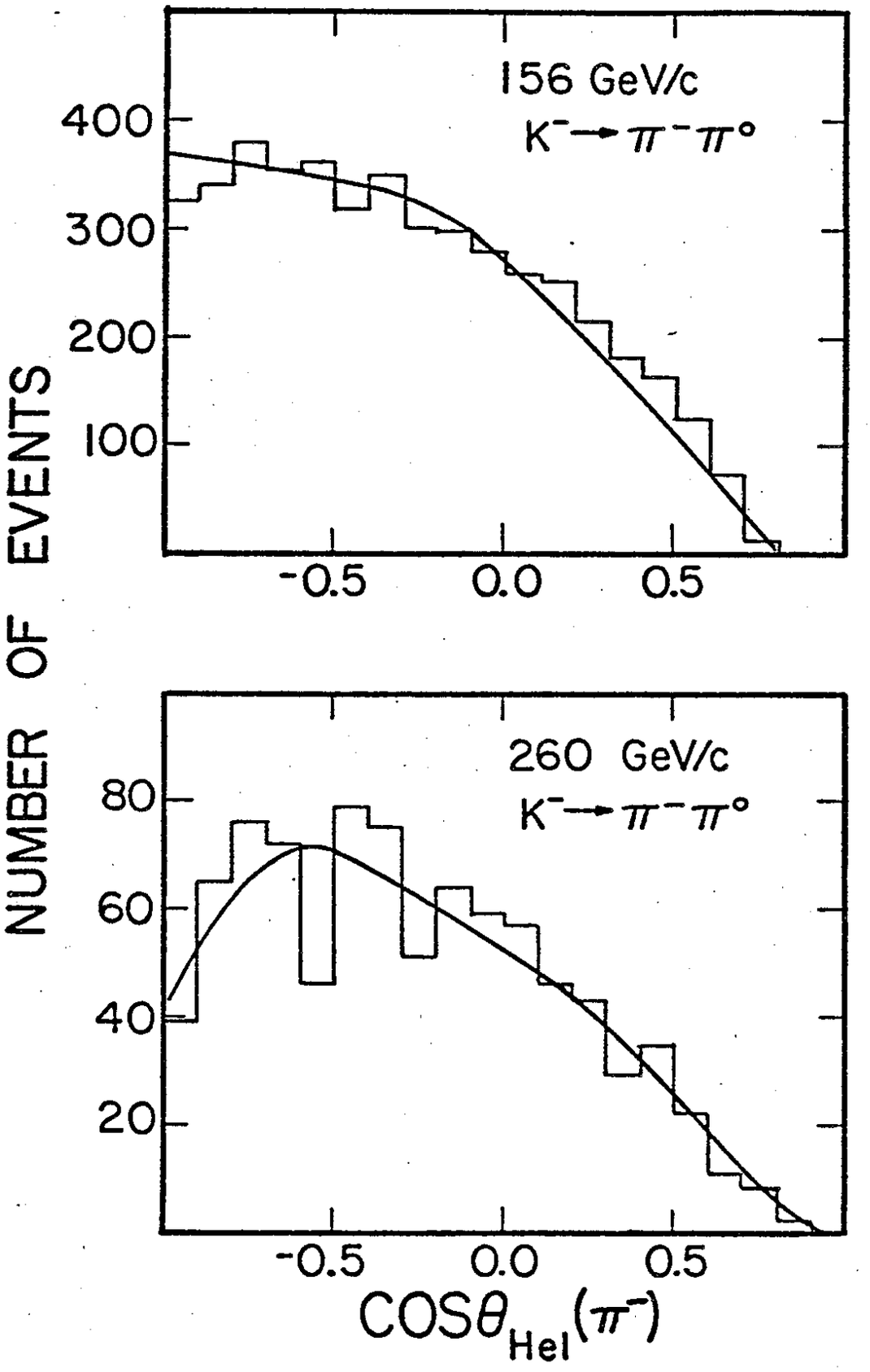
156 GeV/c
K⁻ → π⁻π°
400
300
200
100
-0.5
0.0
0.5
260 GeV/c
K⁻ → π⁻π°
80
60
40
20
-0.5
0.0
0.5
NUMBER OF EVENTS
COSθHel(π⁻)

Fig 12

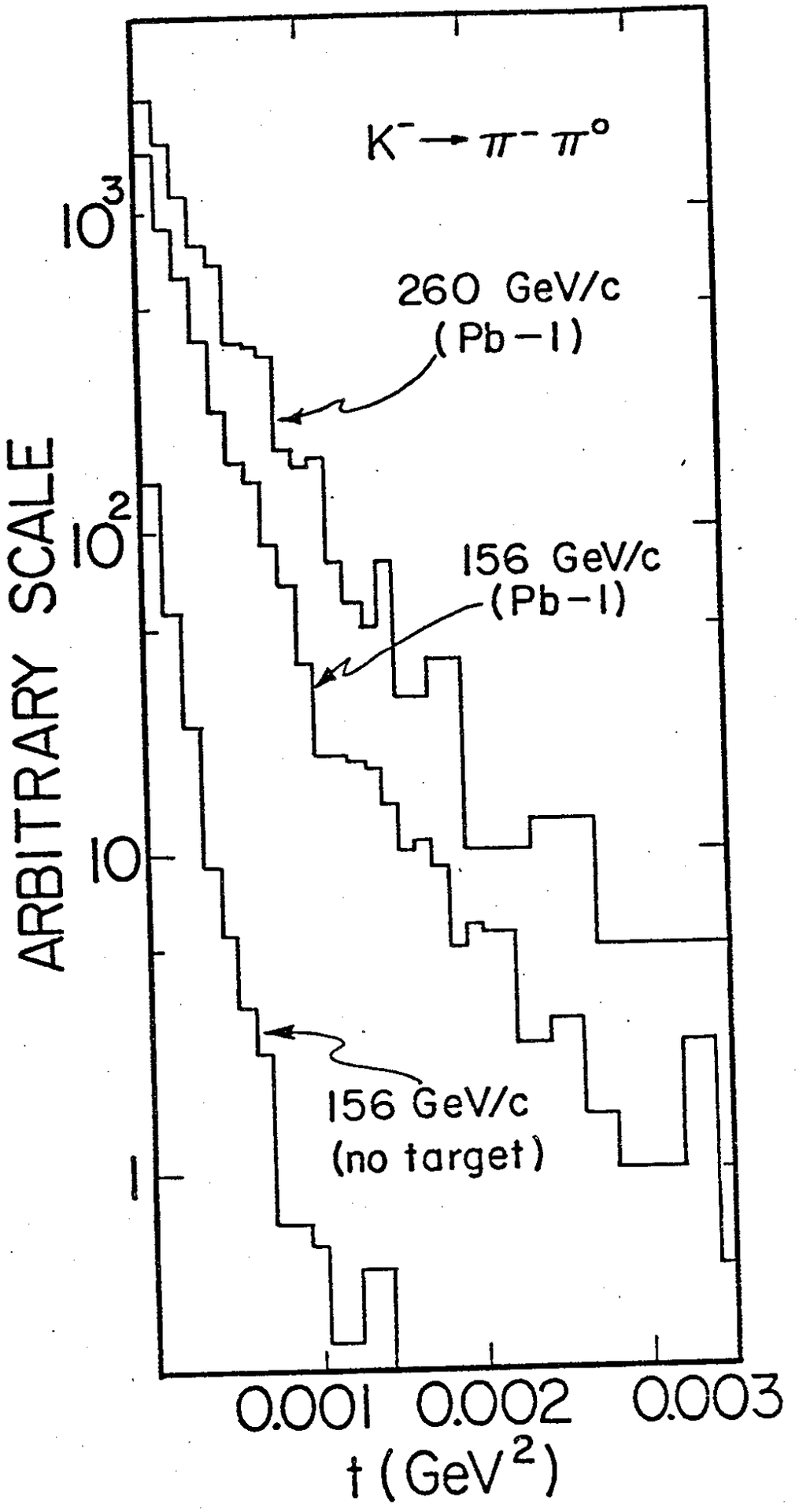
$K^- \rightarrow \pi^- \pi^\circ$
260 GeV/c
(Pb-1)
156 GeV/c
(Pb-1)
156 GeV/c
(no target)
ARBITRARY SCALE
10^3
10^2
10
1
0.001
0.002
0.003
t (GeV^2)

Fig 13

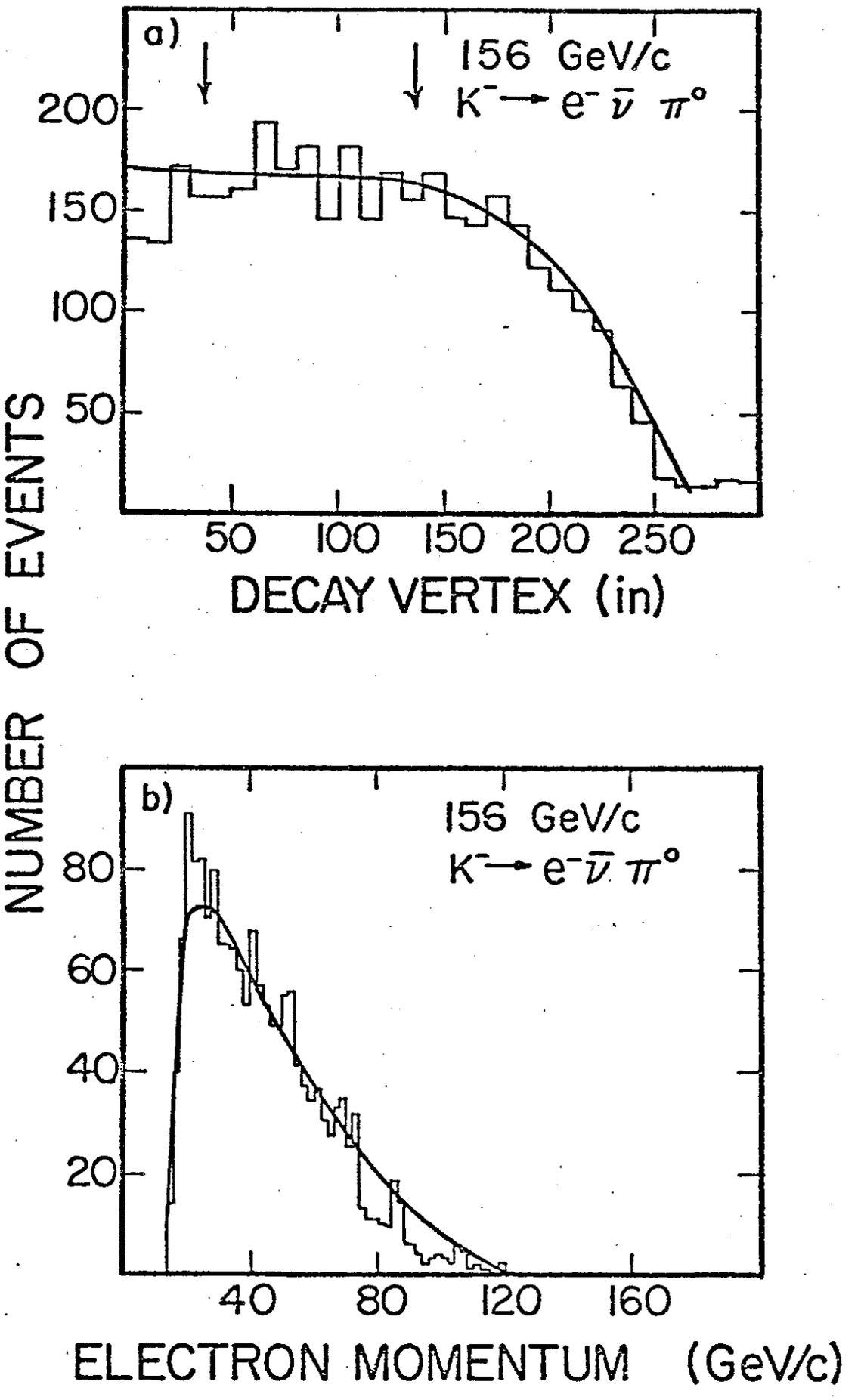
a)
156 GeV/c
$K^- \rightarrow e^- \bar{\nu} \pi^\circ$
200
150
100
50
50 100 150 200 250
DECAY VERTEX (in)
NUMBER OF EVENTS
b)
156 GeV/c
$K^- \rightarrow e^- \bar{\nu} \pi^\circ$
80
60
40
20
40 80 120 160
ELECTRON MOMENTUM (GeV/c)

Fig 14

Fig

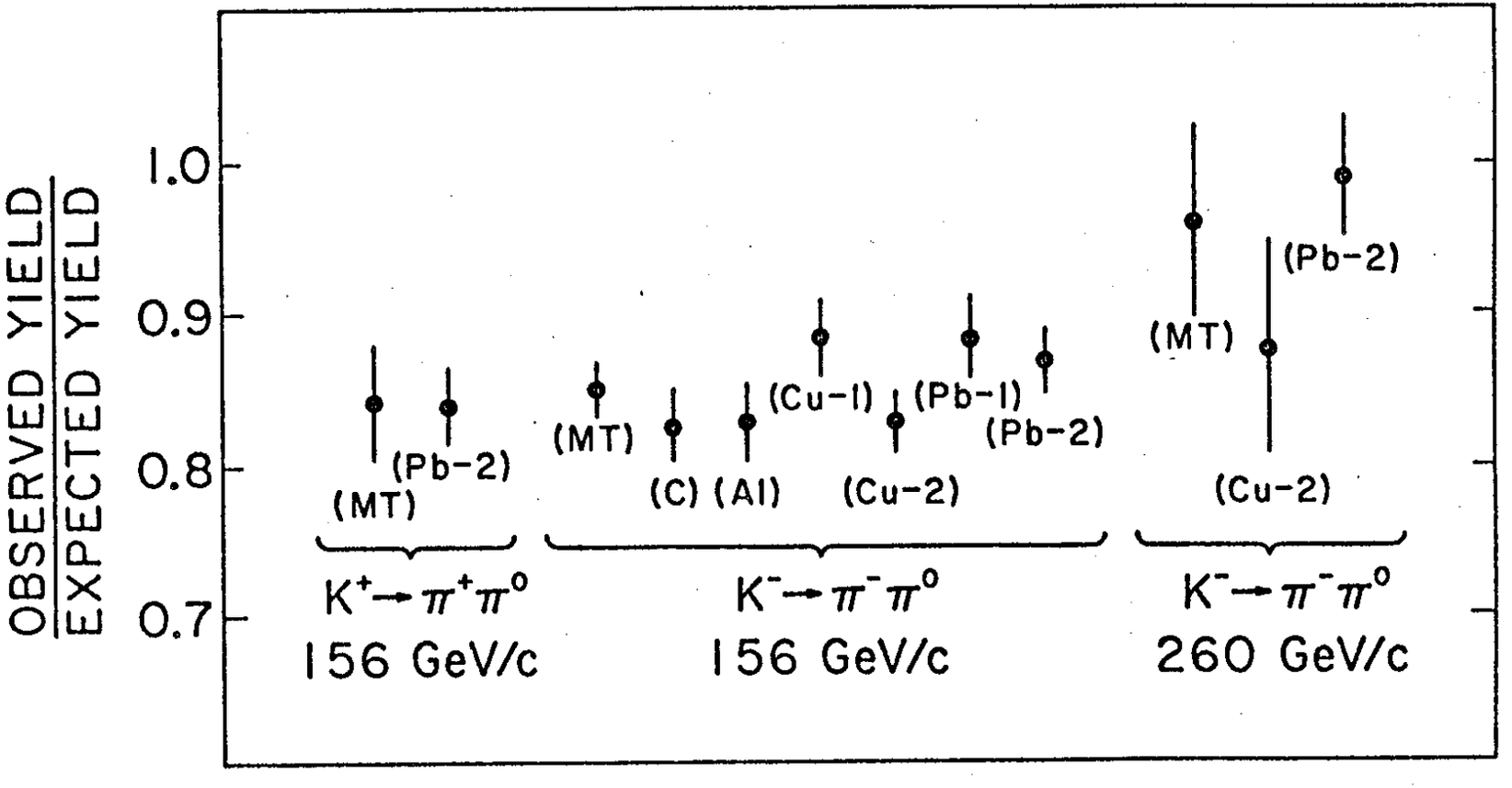
OBSERVED YIELD / EXPECTED YIELD
1.0
0.9
0.8
0.7
(MT)
(Pb-2)
(MT)
(C)
(Al)
(Cu-1)
(Cu-2)
(Pb-1)
(Pb-2)
(MT)
(Cu-2)
(Pb-2)
K⁺→π⁺π⁰
156 GeV/c
K⁻→π⁻π⁰
156 GeV/c
K⁻→π⁻π⁰
260 GeV/c

Fig 15

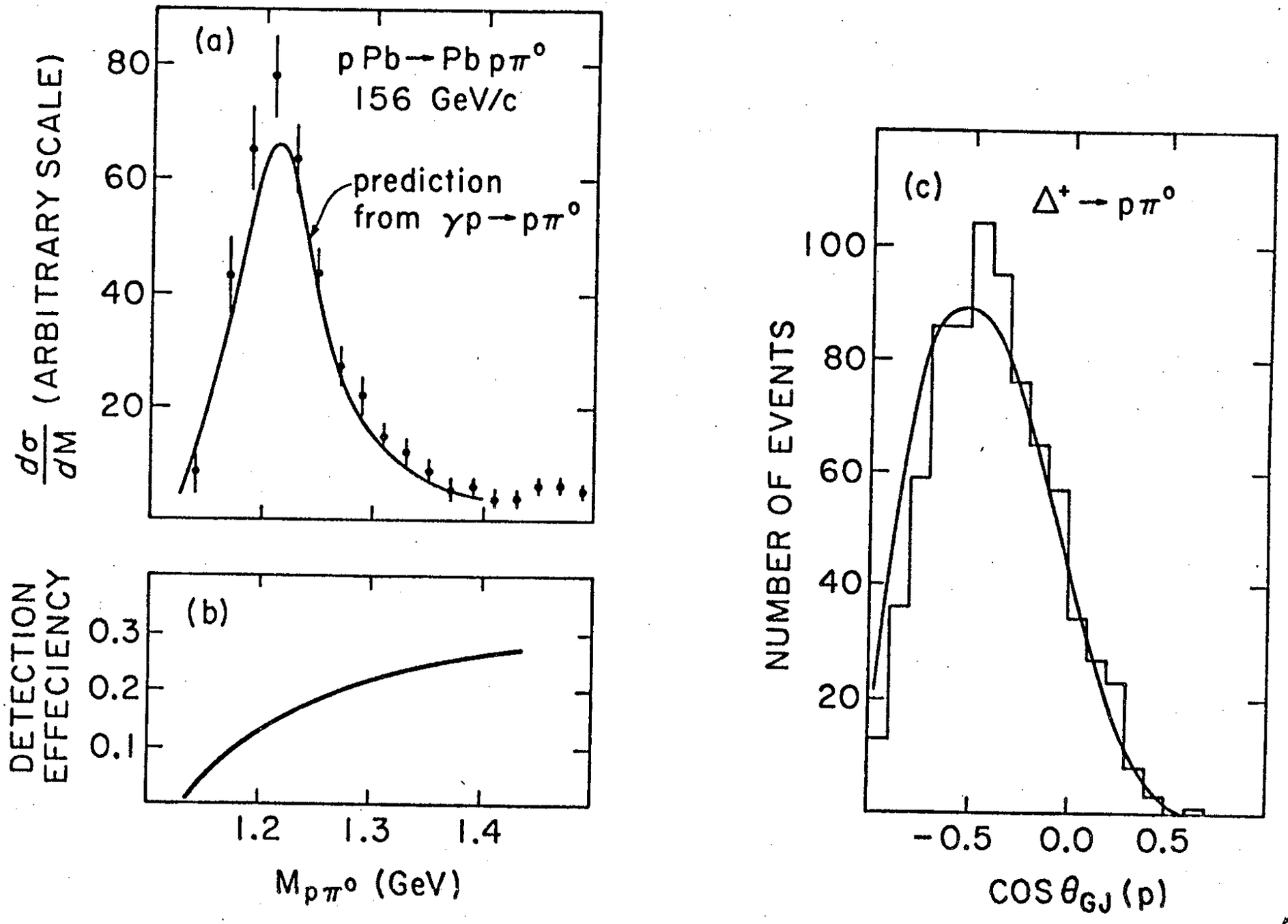
(a)
p Pb → Pb pπ°
156 GeV/c
prediction
from γp → pπ°
dσ/dM (ARBITRARY SCALE)
80
60
40
20
(b)
DETECTION
EFFECIENCY
0.3
0.2
0.1
1.2
1.3
1.4
M pπ° (GeV)
(c)
Δ⁺ → pπ°
NUMBER OF EVENTS
100
80
60
40
20
-0.5
0.0
0.5
COS θGJ (p)

Fig 1

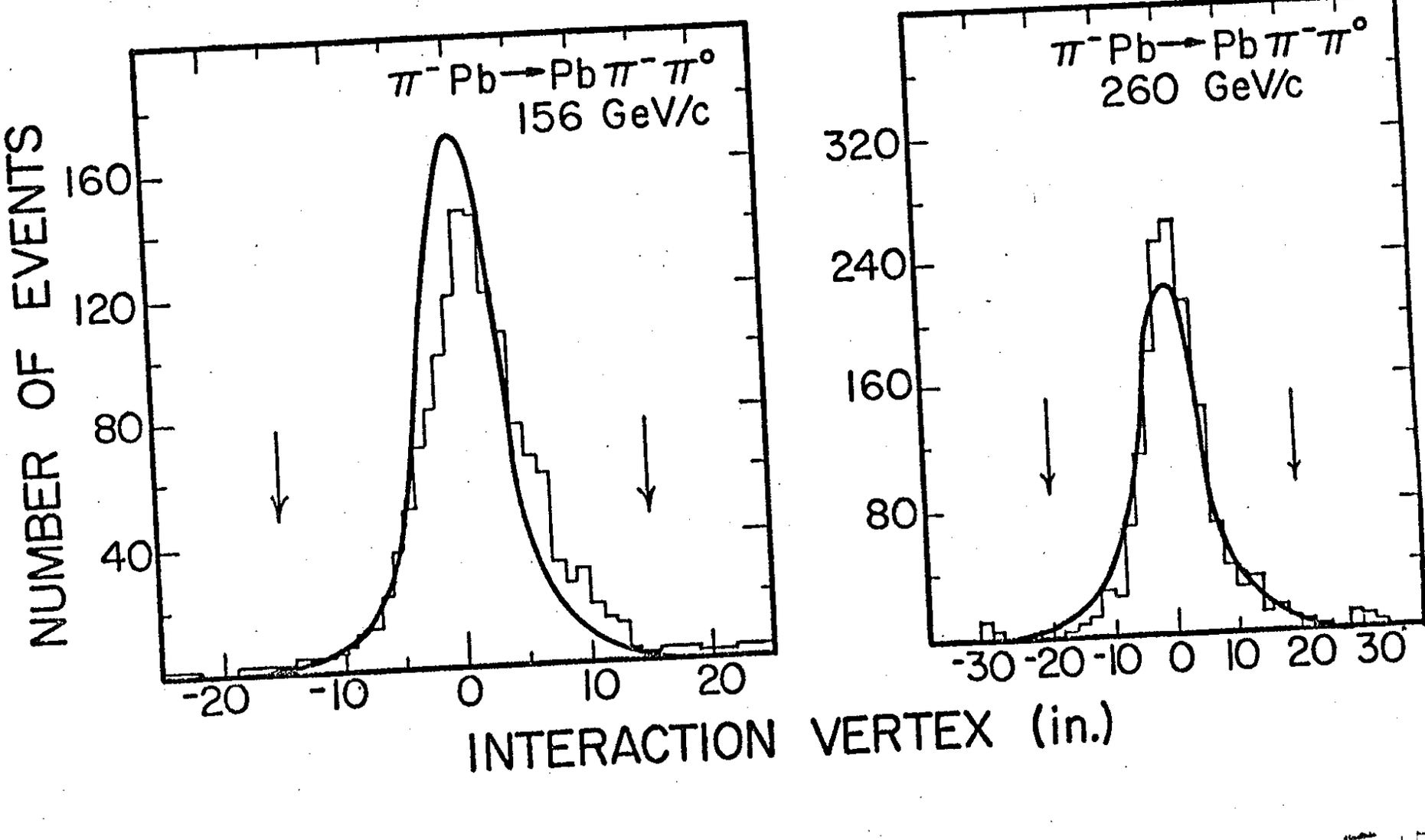
$\pi^- Pb \rightarrow Pb\,\pi^-\pi^\circ$
156 GeV/c
$\pi^- Pb \rightarrow Pb\,\pi^-\pi^\circ$
260 GeV/c
NUMBER OF EVENTS
160
120
80
40
320
240
160
80
-20
-10
0
10
20
-30
-20
-10
0
10
20
30
INTERACTION VERTEX (in.)

Fig 1

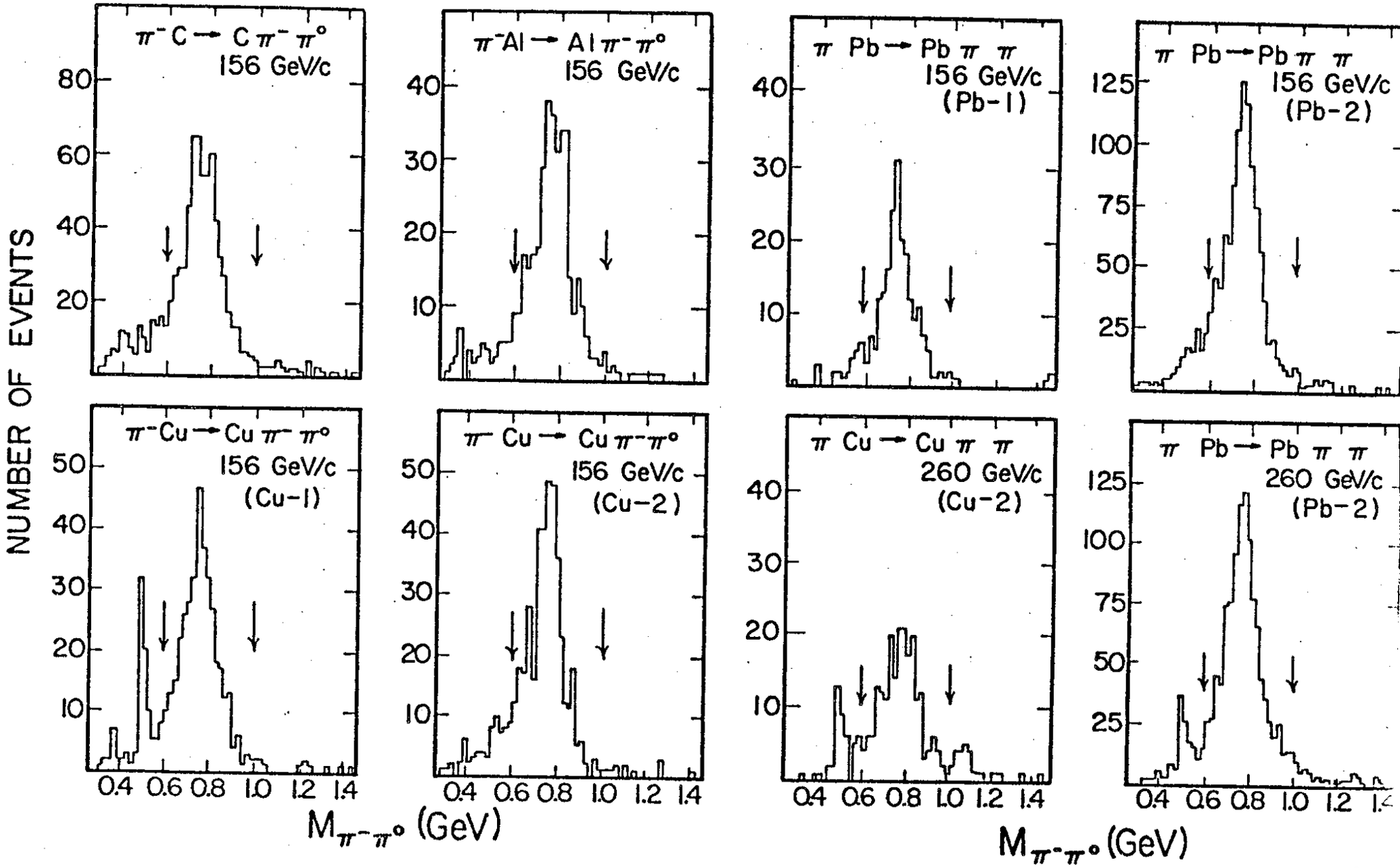
NUMBER OF EVENTS
π⁻ C → C π⁻ π°
156 GeV/c
π⁻ Al → Al π⁻ π°
156 GeV/c
π Pb → Pb π π
156 GeV/c
(Pb-1)
π Pb → Pb π π
156 GeV/c
(Pb-2)
π⁻ Cu → Cu π⁻ π°
156 GeV/c
(Cu-1)
π⁻ Cu → Cu π⁻ π°
156 GeV/c
(Cu-2)
π Cu → Cu π π
260 GeV/c
(Cu-2)
π Pb → Pb π π
260 GeV/c
(Pb-2)
0.4 0.6 0.8 1.0 1.2 1.4
M π⁻ π° (GeV)
M π⁻ π° (GeV)

Fig 18

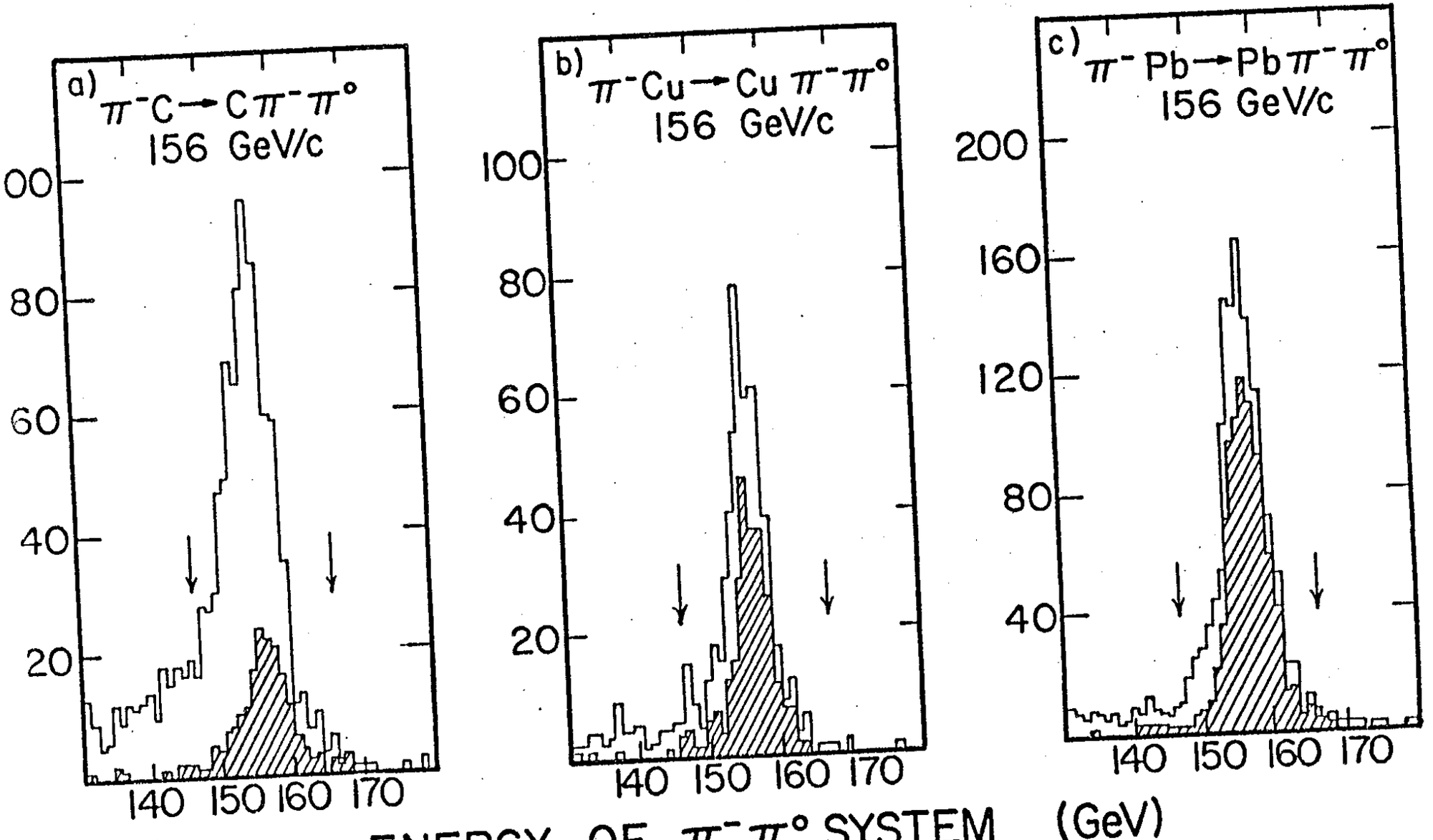
a) $\pi^- C \rightarrow C \pi^- \pi^\circ$
156 GeV/c
b) $\pi^- Cu \rightarrow Cu \pi^- \pi^\circ$
156 GeV/c
c) $\pi^- Pb \rightarrow Pb \pi^- \pi^\circ$
156 GeV/c
00
80
60
40
20
100
80
60
40
20
200
160
120
80
40
140 150 160 170
140 150 160 170
140 150 160 170
ENERGY OF $\pi^- \pi^\circ$ SYSTEM (GeV)

Fig 19

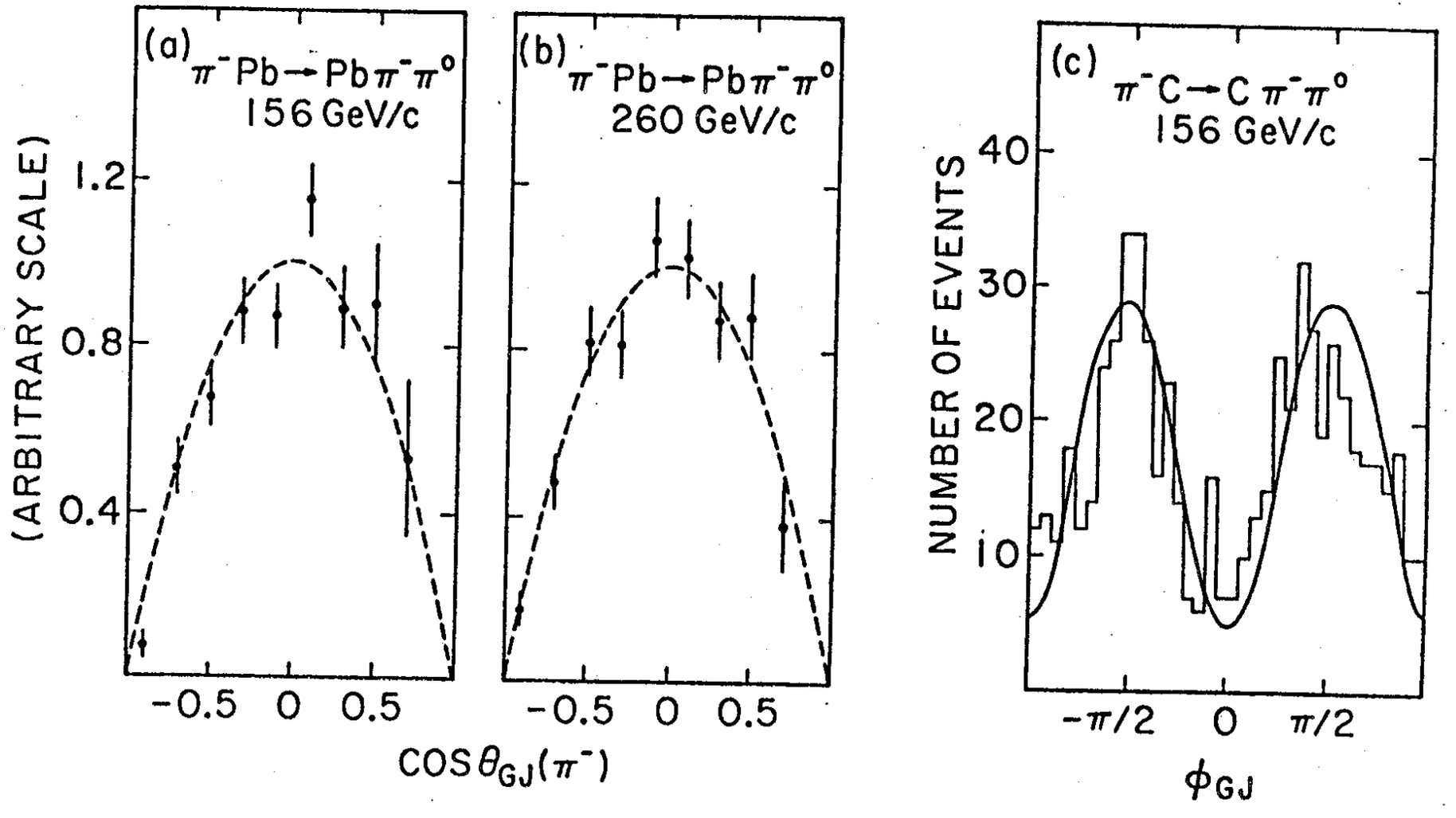
(a) $\pi^- Pb \rightarrow Pb\pi^-\pi^0$
156 GeV/c
(b) $\pi^- Pb \rightarrow Pb\pi^-\pi^0$
260 GeV/c
(ARBITRARY SCALE)
1.2
0.8
0.4
-0.5
0
0.5
$\cos\theta_{GJ}(\pi^-)$
(c) $\pi^- C \rightarrow C\pi^-\pi^0$
156 GeV/c
NUMBER OF EVENTS
40
30
20
10
$-\pi/2$
0
$\pi/2$
ϕ_{GJ}

Fig 20

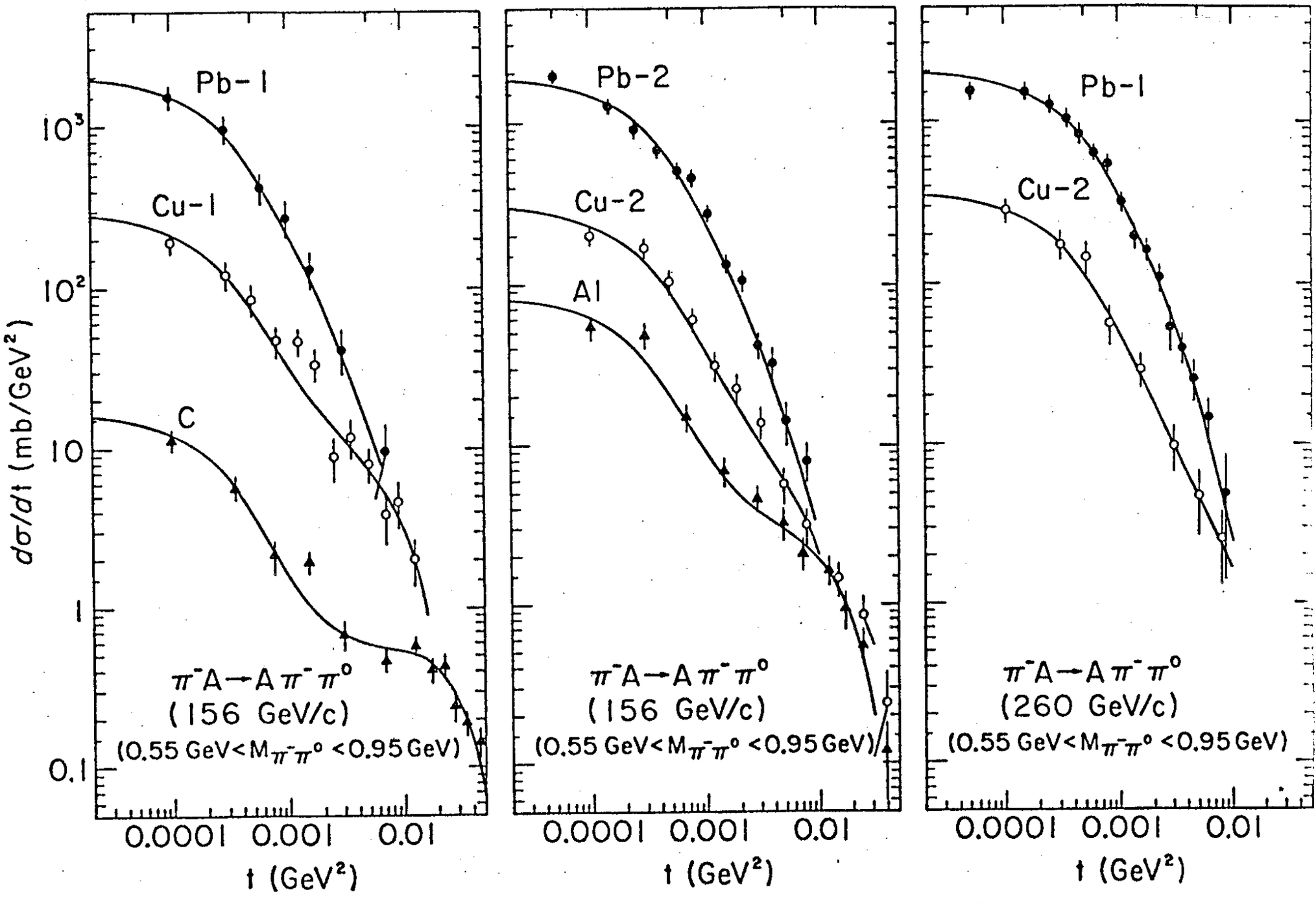
Pb-1
Cu-1
C
Pb-2
Cu-2
Al
Pb-1
Cu-2
$d\sigma/dt$ (mb/GeV^2)
10^3
10^2
10
1
0.1
$\pi^- A \to A \pi^- \pi^0$
(156 GeV/c)
(0.55 GeV< $M_{\pi^-\pi^0}$ <0.95 GeV)
$\pi^- A \to A \pi^- \pi^0$
(156 GeV/c)
(0.55 GeV< $M_{\pi^-\pi^0}$ <0.95 GeV)
$\pi^- A \to A \pi^- \pi^0$
(260 GeV/c)
(0.55 GeV< $M_{\pi^-\pi^0}$ <0.95 GeV)
0.0001 0.001 0.01
t (GeV^2)
0.0001 0.001 0.01
t (GeV^2)
0.0001 0.001 0.01
t (GeV^2)

Fig 21

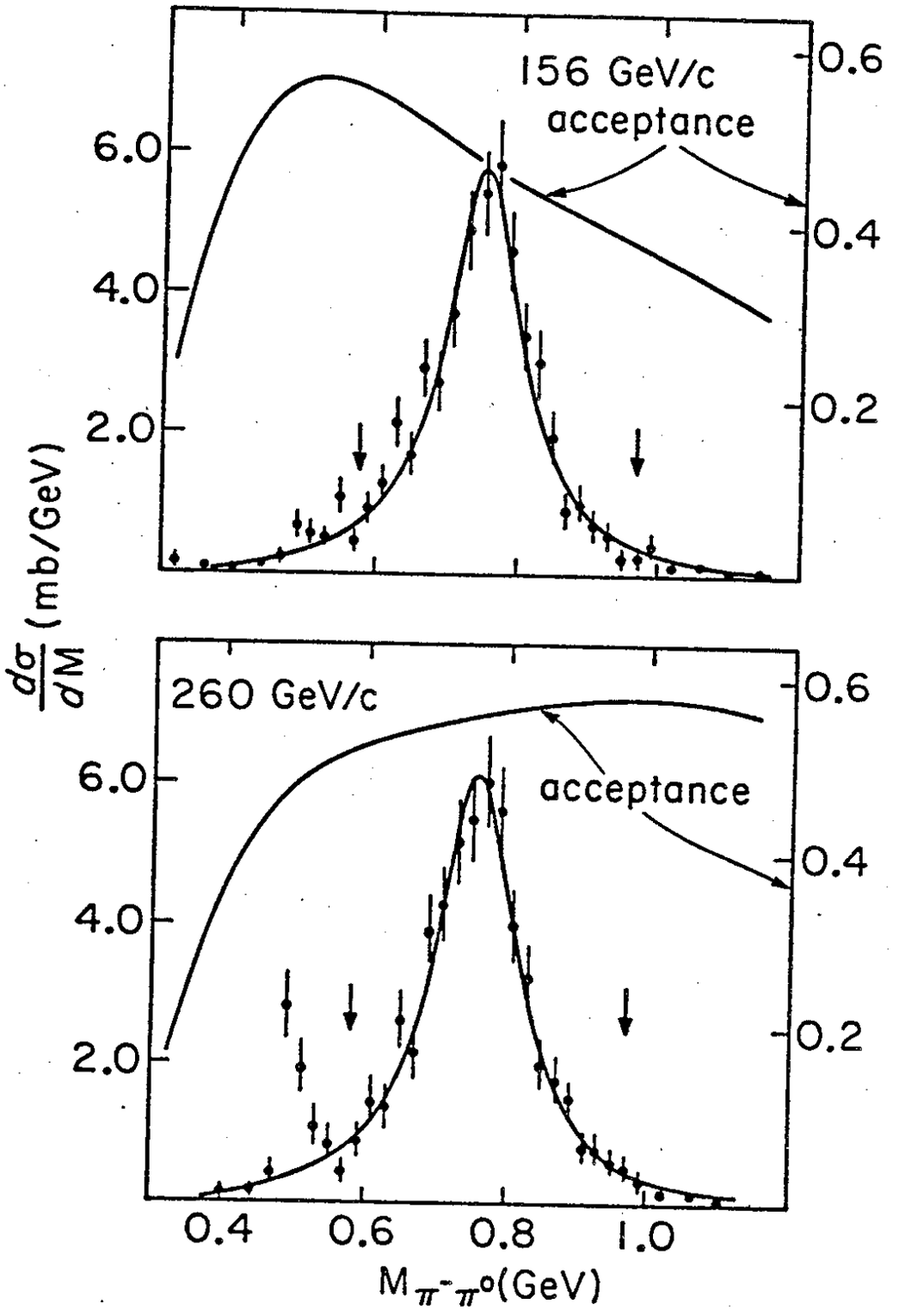
156 GeV/c
acceptance
260 GeV/c
acceptance
6.0
4.0
2.0
0.6
0.4
0.2
$\frac{d\sigma}{dM}$ (mb/GeV)
0.4
0.6
0.8
1.0
$M_{\pi^-\pi^0}$(GeV)

Fig 22

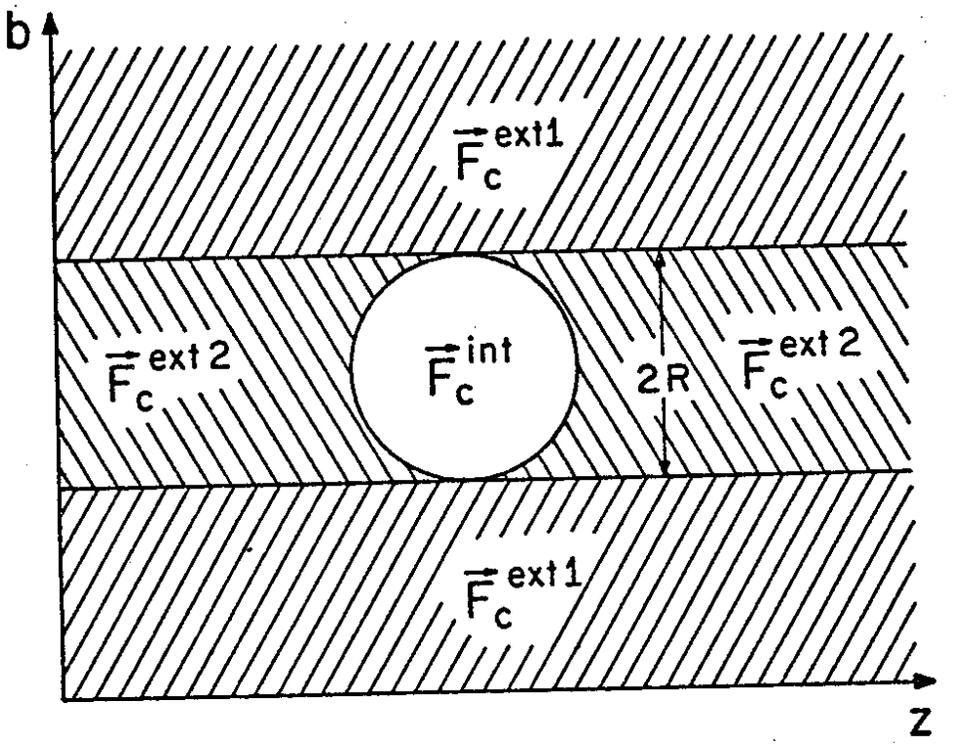

Fig 23

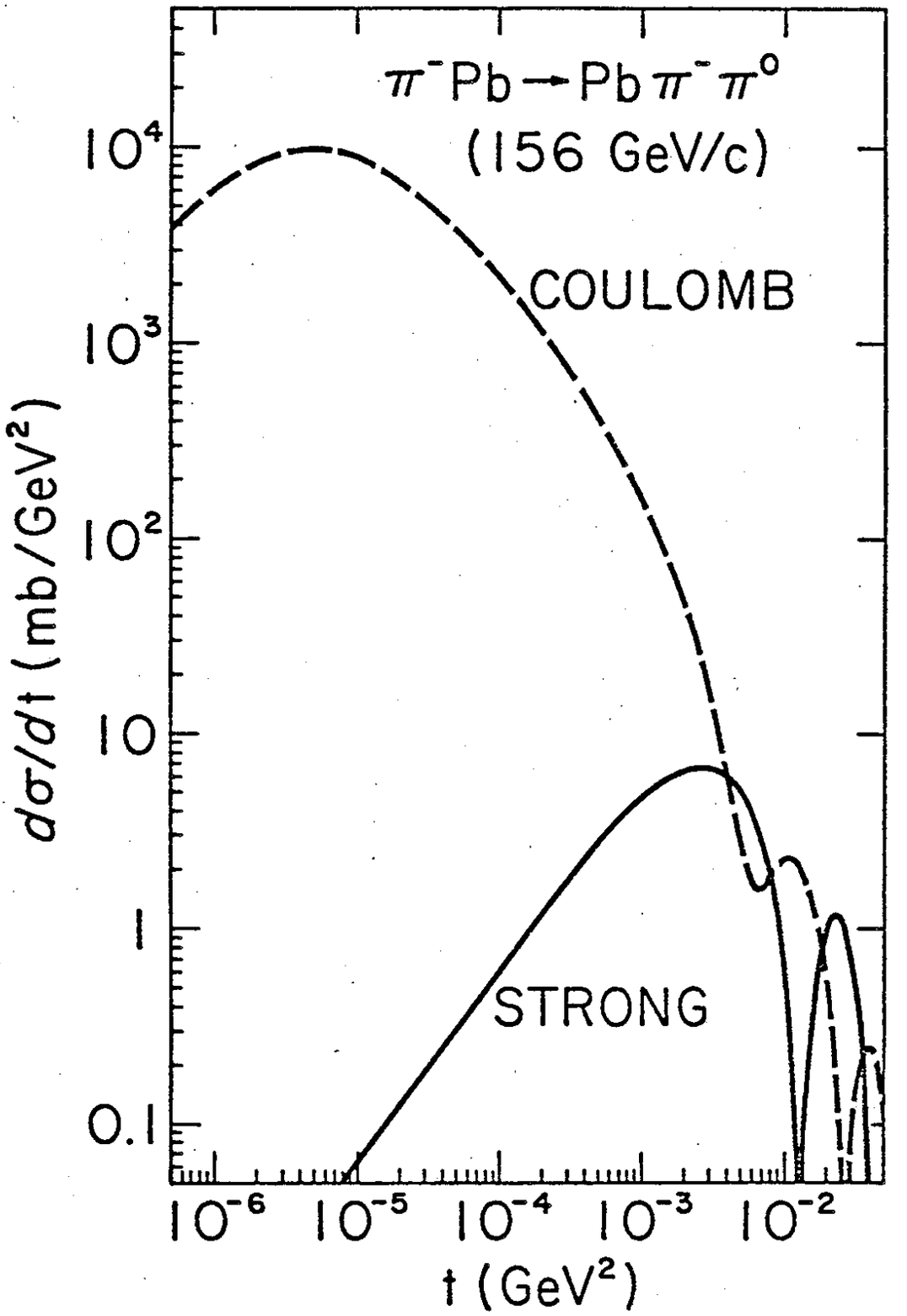
$\pi^- Pb \rightarrow Pb\,\pi^-\pi^0$
(156 GeV/c)
COULOMB
STRONG
$d\sigma/dt$ (mb/GeV^2)
10^4
10^3
10^2
10
1
0.1
10^{-6} 10^{-5} 10^{-4} 10^{-3} 10^{-2}
t (GeV^2)

Fig 24